Node-dependent kinematics approach for progressive damage analysis of pultruded composite structures based on 3D Tsai-Wu damage model

J. Shen [a], M.R.T Arruda [b*], A. Pagani [a], M. Petrolo [a], E. Carrera [a], R. Augello [a], E. Zappino [a],

[a] *Mul*2 Lab, Department of Mechanical and Aerospace Engineering, Politecnico di Torino, Italy
[b] LNEC, National Laboratory of Civil Engineering, Department of Structures - Structural Behaviour Unit, Portugal

Abstract: *This work investigates the progressive damage analysis of pultruded composite structures using the higher-order beam models with Node-Dependent Kinematics (NDK) based on Carrera Unified Formulation (CUF). A three-dimensional (3D) Tsai-Wu orthotropic damage model is implemented, in which the fracture energy and viscous regularization techniques are coupled. Subsequently, three experimental benchmarks involving compact tension, three-point bending, and four-point bending tests on pultruded composite structures are selected to validate the proposed numerical framework. The comparison between numerical and experimental results shows that the numerical framework is able to provide accurate and objective structural responses. Moreover, the use of NDK enhances the computational efficiency of the progressive damage analysis without affecting accuracy.*

Keywords: Damage mechanics; Carrera Unified Formulation; Fracture energy regularization; Viscous regularization; Pultruded composites

1 Introduction

Pultruded composites are Fiber-Reinforced Polymer (FRP) composite material manufactured through the pultrusion process. Due to its high-strength and lightweight nature, this type of composites has been used across a wide range of industries, from aerospace to construction. Composite structures are often prone to complex damage mechanisms such as fiber breakage, matrix cracking, and delamination. These failure modes often develop progressively under quasi-static loading. Therefore, correct design and efficient use of these composite materials require the progressive damage analysis, including the failure onset and propagation.

To overcome the problems related to demanding experimental tests, various numerical models have been widely proposed to analyze the progressive damage of composite structures. The first challenge is to select the suitable failure criterion. There are many failure theories in

*Corresponding author. E-mail: mario.rui.arruda@tecnico.ulisboa.pt

the literature, such as Tsai-Wu [1], Hashin [2], and Puck [3]. Despite their success in predicting the failure of composite structures, these models have been observed to underestimate the experimental strength when applied to pultruded FRP elements [4, 5], as they neglect the progressive damage. Therefore, it is necessary to take damage propagation into account in the failure analysis.

In Continuum Damage Mechanics (CDM), the damage propagation indicates the degradation of elastic moduli due to the growth and coalesce of voids or micro-cracks. An exponential damage evolution model coupled with a failure initiation criterion was first proposed in [6], and is commonly referred to as the Matzenmiller–Lubliner–Taylor (MLT) model. The MLT model produces reasonably accurate results [7], but requires the parameterization of damage coefficients that control the 'smoothness' of damage evolution. A decohesion Finite Element (FE) was developed by [8] as an alternative method for simulating delamination between solid elements using a mixed-mode progressive damage model. Their formulation incorporated a strain-softening behavior governed by fracture energy, which was previously applied to concrete [9]. Compared to MLT, this method offers the advantage of employing physically meaningful parameters, such as fracture energies. However, the experimental determination of fracture energies for each failure mode is difficult. Moreover, the fracture energies measured may exhibit a wide range for similar materials [10, 11, 12].

Nevertheless, some of the aforementioned models were included in commercial software, and were widely utilized in numerical analysis. A damage initiation and progression model, presented in [13] and based on the works of Hashin [2], MLT [6], and decohesion [8], is included in ABAQUS. Recently, a two-dimensional (2D) orthotropic damage model based on the Tsai–Wu failure criterion was developed in [14, 15], in which failure modes can be identified once the criterion is met.

The previous 2D orthotropic damage models are only limited to shell elements due to their transverse isotropic assumption [16]. Moreover, classical lower-order structural theories have been reported to be insufficient for progressive failure analysis in composite laminates [17]. Thus, high-fidelity simulations necessitate the incorporation of three-dimensional (3D) orthotropic damage models based on appropriate failure criteria into solid elements. For instance, the Hashin failure criterion has been extended to 3D applications, as presented in [18], though interlaminar damage was not considered. Practical implementation of the LaRC05 failure criterion and its variations for 3D analysis was explored in [19, 20]. In [21], a fully 3D formulation of the Hashin criterion was demonstrated coupled with simplified degradation models, tailored for bolted connections.

The development of 3D composite constitutive relations is also associated with the need for simulating connections, mainly with bolts [20, 22]. Certain damage models are capable of predicting not only the failure of FRP laminates, but also their post-failure behavior [23]. However, these models often require high-density meshes and significant computational resources, primarily due to the need to resolve individual plies and/or implement cohesive interfaces [24], making them impractical for the analysis of large-scale engineering problems. Some authors have chosen novel formulations [25] using standard concepts that couple the damage initiation between the fiber, matrix and interlaminar to successfully simulate composites beam-column connections [26]. Recently, a 3D orthotropic damage model based on 3D Hashin failure including interlaminar failure was proposed in [27]. Moreover, the 2D Tsai-Wu damage model [14] was extended to 3D in which the interlaminar failure is included in [28]. In [27, 28], fracture energy regularization was employed to mitigate the mesh dependency and viscous regularization was utilized to alleviate the convergence issues.

Although the aforementioned 3D models can obtain accurate results, the computational

costs can increase significantly. Carrera Unified Formulation (CUF) [29] provide an alternative solution for 3D solid elements. In the CUF framework, 3D displacement fields of an one-dimensional (1D) beam model can be obtained through cross-sectional expansion functions. Higher-order beam models allow for accurate failure analyses since accurate stresses and strains can be recovered [29]. CUF has been successfully applied for the damage analysis of concrete and reinforced concrete structures [30, 31]. Moreover, it has also been exploited for composite laminates [32, 33], in which the CODAM2 model [34] was integrated into 2D CUF-based layer-wise models. Recently, the 3D orthotropic damage model based on 3D Hashin failure criterion was implemented in the CUF-based beam models for composite structures [35].

In CUF, the Node-Dependent Kinematics (NDK) approach [36] allows the employment of different cross-sectional kinematics within the same beam model. With the help of this approach, the structure can be divided into critical zones with refined models and non-critical zones with lower-order models so that the computational costs can be further reduced without sacrificing accuracy. This approach was investigated for the analysis of composite structures [37, 38, 39], most of which are limited to the linear static analysis [40].

This work aims to apply the CUF-based higher-order beam models to the progressive damage analysis of pultruded composite structures. In addition to the novelties stemmed from previous works [32, 35], this work employs a new orthotropic damage model based on 3D Tsai-Wu failure criterion in which only one single scalar failure surface is needed and different failure modes can be distinguished at the onset of failure. Moreover, this work aims to mitigate the mesh dependency more effectively through a new characteristic element length from [41]. Additionally, the viscous regularization, which was ignored in the previous works, is implemented in this work to mitigate the convergence difficulties, especially for brittle failure case. This work employs the NDK approach to enhance the computational efficiency of CUF-based beam models in the progressive damage analysis of pultruded composite structures for the first time.

The paper is organized as follows: Section 2 introduces the fundamentals of CUF-based models with NDK briefly; Section 3 presents a novel orthotropic damage model based on 3D Tsai-Wu failure criterion, in which the fracture energy regularization and viscous regularization techniques are introduced; Subsequently, Section 4 illustrates and discusses three numerical examples. Finally, Section 5 draws the conclusions.

2 Unified higher-order finite beam elements

In this section, higher-order beam theories based on CUF are briefly introduced. As shown in Fig. 1, this theory overcomes the assumption of rigid cross-sections in a 1D domain by approximating the 3D displacement field through the following equation:

$$\mathbf{u}(x, y, z) = F_\tau(x, z)\mathbf{u}_\tau(y), \qquad \tau = 1, 2, ..., M \tag{1}$$

where y is the axial direction of the beam, and x and z are the cross-sectional coordinates; $\mathbf{u}_\tau(y)$ denotes the generalized displacements along the axial direction; $F_\tau(x, z)$ is the cross-sectional expansion function; τ represents a summation over terms, and M denotes the number of terms in cross-sectional expansion functions.

The displacement of the beam model in the 1D case along the axial direction can be approximated using the finite element shape functions $N_i(y)$, as shown in Fig. 1, which includes different beam elements of linear (B2), quadratic (B3), and cubic (B4) orders. Therefore, Eq.

(1) can be expressed as:

$$\mathbf{u}(x, y, z) = F_\tau(x, z) N_i(y) \mathbf{u}_{\tau i}, \qquad i = 1, ..., N_{NE} \tag{2}$$

where N_{NE} denotes the number of nodes per beam element; $\mathbf{u}_{\tau i}$ is the nodal displacement vector.

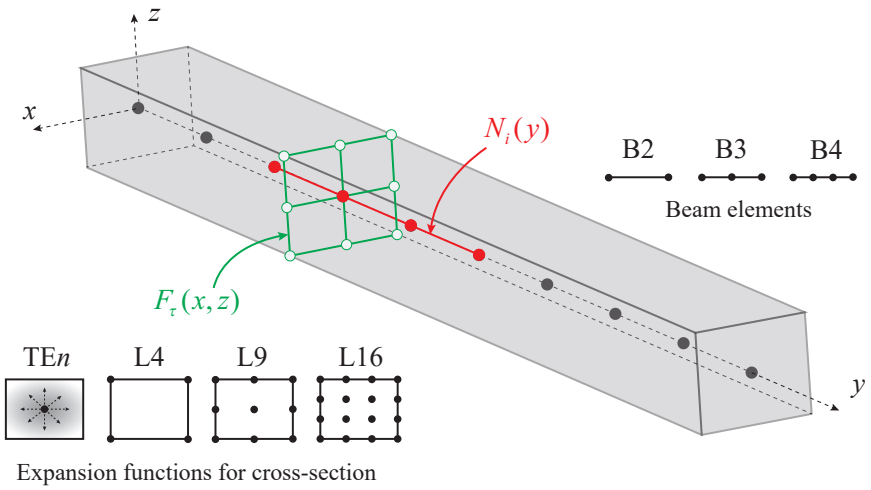

Figure 1: Reference framework, beam elements, and cross-section expansion

2.1 Cross-sectional expansions

Various types of F_τ such as polynomials, harmonics, and exponentials can be implemented through CUF. The choice of a particular expansion characterizes the capabilities of a structural theory: the richer the expansion, the more accurate the results [29]. The most commonly implemented Taylor-like and Lagrange polynomial expansions, as shown in Fig. 1, are briefly introduced below.

Taylor-like polynomials consists of the 2D base $x^i z^j$, where i and j are positive integers. The 1D beam model based on such polynomials is referred to as TEn model, where n denotes the expansion order. For instance, the complete quadratic (i.e., $n = 2$) Taylor-like polynomial basis takes the form: $F_1 = 1$, $F_2 = x$, $F_3 = z$, $F_4 = x^2$, $F_5 = xz$, $F_6 = z^2$. Then, the displacement field can be expressed as follows:

$$\begin{aligned} u_x =& u_{x1} + x u_{x2} + z u_{x3} + x^2 u_{x4} + xz u_{x5} + z^2 u_{x6} \\ u_y =& u_{y1} + x u_{y2} + z u_{y3} + x^2 u_{y4} + xz u_{y5} + z^2 u_{y6} \\ u_z =& u_{z1} + x u_{z2} + z u_{z3} + x^2 u_{z4} + xz u_{z5} + z^2 u_{z6} \end{aligned} \tag{3}$$

where $u_{x1} \cdots u_{z3}$ are unknown variables. It is important to note that classical beam theories, such as Euler-Bernoulli and Timoshenko, are special cases of TE1-based 1D CUF models.

Similarly, 1D CUF models based on 2D Lagrange polynomial expansions can be referred to as LE models. Based on the order of Lagrange polynomials, the options of quadrilateral elements include bilinear four-point (L4), quadratic nine-point (L9), and cubic sixteen-point

(L16). The expression for one L9 element is shown here as an example:

$$
\begin{aligned}
F_\tau =& \frac{1}{4}\left(r^2+rr_\tau\right)\left(s^2+ss_\tau\right), \quad \tau = 1,3,5,7 \\
F_\tau =& \frac{1}{2}s_\tau^2\left(s^2+ss_\tau\right)\left(1-r^2\right)+\frac{1}{2}r_\tau^2\left(r^2+rr_\tau\right)\left(1-s^2\right), \quad \tau = 2,4,6,8 \\
F_\tau =& \left(1-r^2\right)\left(1-s^2\right), \quad \tau = 9
\end{aligned}
\tag{4}
$$

where (r, s) are the normalized coordinates, while (r_τ, s_τ) represent the normalized coordinates of each node τ.

Compared to TE models, unknown variables of LE models, which are pure displacement components, can be located above the physical surfaces of the structure. Moreover, locally refined models can be easily built using LE.

2.2 Node-dependent kinematics

The Node-dependent kinematics approach was first proposed in [37] to mix different structural theories in the CUF framework. The key idea is allowing for different kinematics at each node of a 1D beam element, which works as a transition to connect elements with different kinematics without any displacement discontinuities. As seen in Fig. 2, the whole domain is divided into two zones where two different cross-sectional kinematics are employed. A transition element with node-dependent kinematics is used to connect these two zones. The kinematics description of each point in this transition element is independent, and they are smeared by the shape functions that ensure a smooth transition between the displacement of the two nodes. Therefore, the displacement continuity can be guaranteed between two zones without any need for special coupling techniques.

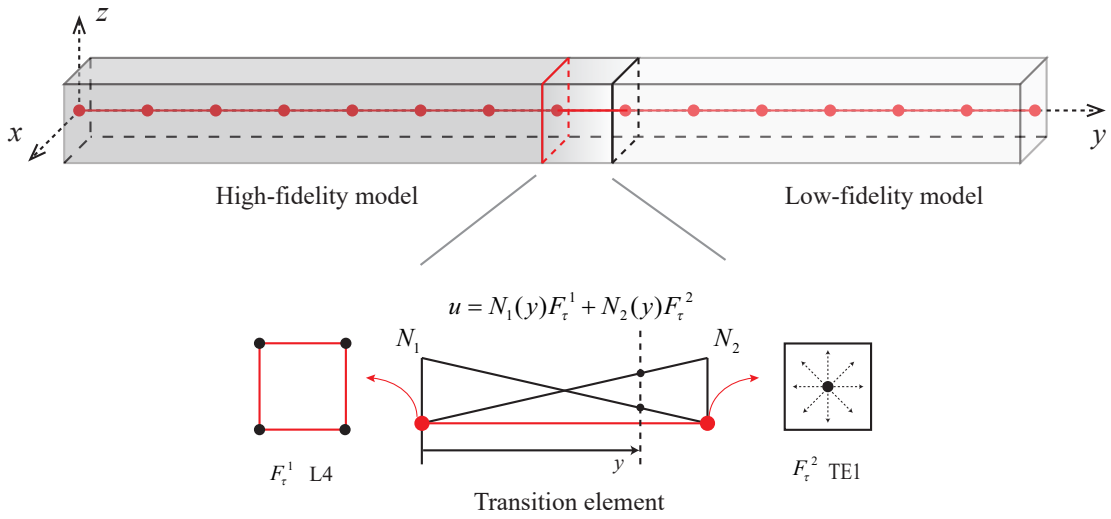

Figure 2: NDK approach for beams

This idea can be easily extended to any order beam models in CUF. In general, the displacement field of 1D element with node-dependent kinematics can be rewritten as:

$$
\mathbf{u}(x,y,z) = F_\tau^i(x,z)N_i(y)\mathbf{u}_{\tau i}, \qquad \tau = 1,...,M^i \qquad i = 1,...,N_{NE} \tag{5}
$$

where F_τ^i represents the expansion function at node point i and M^i is the corresponding number of expansion terms.

With NDK, the numerical accuracy can be improved using a refinement in the kinematics assumptions without mesh refinement of FE model. Furthermore, a balance between accuracy and computational costs can be achieved where refined models can be employed for the selected zones of interest such as critical zones vulnerable to damage and coarse models can be adopted for the non-critical regions of the structure. In the present work, the critical regions are modelled using LE, while the remaining structure is modelled using lower-order TE.

2.3 Governing equations

The governing equations can be derived using the Principle of Virtual Displacement (PVD) which assumes that the external virtual work (δL_{ext}) is equal to the internal virtual work (δL_{int}) in the static case.

The internal and external virtual work can be written as:

$$\delta L_{\text{int}} = \int_V \delta\boldsymbol{\varepsilon}^{\mathrm{T}}\boldsymbol{\sigma}\,\mathrm{d}V \tag{6}$$

$$\delta L_{\text{ext}} = \int_V \delta\mathbf{u}^{\mathrm{T}}\mathbf{P}\,\mathrm{d}V \tag{7}$$

where $\boldsymbol{\varepsilon}$ and $\boldsymbol{\sigma}$ are stress and strain vectors, respectively; $\mathbf{P}$ is the external load.

The relationship between displacement and strain fields can be obtained from the geometrical relation:

$$\boldsymbol{\varepsilon} = \mathbf{D}\mathbf{u} \tag{8}$$

where $\mathbf{D}$ is a differential operator. Moreover, the constitutive law permits to derive the relation between stress and strain fields which is expressed as:

$$\boldsymbol{\sigma} = \mathbf{C}^{\mathrm{d}}\boldsymbol{\varepsilon} \tag{9}$$

where $\mathbf{C}^{\mathrm{d}}$ is the 6×6 material stiffness matrix including damage.

Substituting Eq. (8) and (9) and the displacement field given in Eq. (5) into the Eq. (6), the internal virtual work can be rewritten as:

$$\begin{aligned}\delta L_{\text{int}} &= \delta\mathbf{u}_{sj}^{\mathrm{T}} \int_V \left[N_j(y)F_s^j(x,z)\mathbf{D}^{\mathrm{T}}\mathbf{C}^{\mathrm{d}}\mathbf{D}F_\tau^i(x,z)N_i(y)\right]\mathrm{d}V\mathbf{u}_{\tau i} \\ &= \delta\mathbf{u}_{sj}^{\mathrm{T}}\mathbf{K}^{ij\tau s}\mathbf{u}_{\tau i}\end{aligned} \tag{10}$$

where $\mathbf{K}^{ij\tau s}$ is a 3×3 matrix denoted as Fundamental Nucleus (FN), which enables the assembly of the element stiffness matrix independently of the structural theory order. The explicit expression of $\mathbf{K}^{ij\tau s}$ can be found in [37]. For the sake of clarity, the first component $k_{xx}^{ij\tau s}$ is reported:

$$\begin{aligned}k_{xx}^{ij\tau s} = &\int_V C_{11}^{\mathrm{d}}\frac{\partial}{\partial x}\left(N_jF_s^j\right)\frac{\partial}{\partial x}\left(N_iF_\tau^i\right)dV + \int_V C_{16}^{\mathrm{d}}\frac{\partial}{\partial x}\left(N_jF_s^j\right)\frac{\partial}{\partial y}\left(N_iF_\tau^i\right)dV \\ &+ \int_V C_{44}^{\mathrm{d}}\frac{\partial}{\partial z}\left(N_jF_s^j\right)\frac{\partial}{\partial z}\left(N_iF_\tau^i\right)dV + \int_V C_{16}^{\mathrm{d}}\frac{\partial}{\partial y}\left(N_jF_s^j\right)\frac{\partial}{\partial x}\left(N_iF_\tau^i\right)dV \\ &+ \int_V C_{66}^{\mathrm{d}}\frac{\partial}{\partial y}\left(N_jF_s^j\right)\frac{\partial}{\partial y}\left(N_iF_\tau^i\right)dV\end{aligned} \tag{11}$$

Similarly, the external virtual work can be rewritten as Eq. (12) with the introduction of Eq. (5).

$$\delta L_{\text{ext}} = \delta \mathbf{u}_{sj}^{\mathrm{T}} \int_V \delta N_j(y) F_s^j(x,z) \mathbf{P} \mathrm{d}V = \delta \boldsymbol{u}_{sj}^{\mathrm{T}} \mathbf{P}_{sj} \tag{12}$$

where $\mathbf{P}_{sj}$ is the external load acting on beam node j and cross-sectional node s.

Then, the governing equation for static problems is derived by applying the PVD and integrating Eq. (10) with Eq. (12), yielding:

$$\mathbf{K}^{\tau sij} \mathbf{u}_{\tau i} = \mathbf{P}_{sj} \tag{13}$$

2.4 Implicit solution for physical nonlinearity

This work involves physical nonlinearity due to damage. The nonlinear equilibrium equation derived from the CUF-based beam formulation is solved using an implicit displacement-based iterative scheme. At each pseudo-time step $t + \Delta t$, the residual force is expressed as:

$$\mathbf{R}(t + \Delta t) = \mathbf{F}_{\text{ext}}(t + \Delta t) - \mathbf{F}_{\text{int}}(t) \tag{14}$$

where $\mathbf{F}_{\text{int}}(t)$ is the internal force evaluated using current damage state at time t; $\mathbf{F}_{\text{ext}}(t+\Delta t)$ is the applied external load at time $t+\Delta t$; $\mathbf{R}(t+\Delta t)$ is the unbalanced force at the beginning of the increment.

At each time step, the displacement increment Δu is computed by solving the following linear system:

$$\mathbf{K}_{\text{sec}}(t + \Delta t) \cdot \Delta \mathbf{u} = \mathbf{R}(t + \Delta t) \tag{15}$$

in which $\mathbf{K}_{\text{sec}}(t + \Delta t)$ is the secant stiffness matrix constructed based on the damage at time $t + \Delta t$. In the CUF framework, Eq. (15) reads:

$$\mathbf{K}_{\text{sec}}^{\tau sij} \Delta \mathbf{u}_{\tau i} = \mathbf{r}_{sj} \tag{16}$$

where $\mathbf{K}_{\text{sec}}^{\tau sij}$ is the FN of the secant stiffness matrix involving damage, and $\mathbf{r}_{sj}$ is the FN of the residual force vector.

After solving the Eq. (15) or (16), the displacement is updated as $\mathbf{u}(t+\Delta t) = \mathbf{u}(t) + \Delta \mathbf{u}$. The internal force vector and damage variables are then recomputed accordingly. Due to the nonlinearity introduced by damage evolution, the solution generally does not converge within a single step. Therefore, multiple iterations are performed within each time increment. Convergence is checked based on the relative norm of the iterative displacement correction with respect to the accumulated increment:

$$\frac{\|\Delta \mathbf{u}^k\|}{\|\mathbf{u}^k - \mathbf{u}^0\|} < \varepsilon \tag{17}$$

where $\Delta \mathbf{u}^k = \mathbf{u}^k - \mathbf{u}^{k-1}$ is the displacement correction at iteration k, and $\mathbf{u}^0$ is the displacement at the beginning of the current time step t.

In this modified Newton-Raphson method, the secant stiffness matrix is adopted instead of tangent stiffness due to its straightforward implementation. Both the secant stiffness matrix and the internal force vector at each iteration are dependent on the damage state, which is evaluated using the damage model introduced in the following section.

3 3D Tsai-Wu damage model

This section introduces the local orthotropic damage model for composite materials, in which fiber, matrix, interlamina, and shear damage states are taken into account. The corresponding constitutive equations, 3D Tsai-Wu failure criteria, and its related damage evolution law are presented. Fracture energy regularization for higher-order beam elements is employed to mitigate the mesh dependency.

3.1 Damaged material response

Damage caused by a series of microcrakcs or microvoids is often physically considered as the loss of stiffness in the CDM theory [42]. The tensile damage and compressive damage are activated using the effective stress $\hat{\boldsymbol{\sigma}}$. Based on the idea of the model of [6], the relation between the effective stress, $\hat{\boldsymbol{\sigma}}$, and the nominal stress, $\boldsymbol{\sigma}$, is proposed as:

$$\hat{\boldsymbol{\sigma}} = \mathbf{M}\boldsymbol{\sigma} \tag{18}$$

where $\mathbf{M}$ is the damage operator, which is expressed considering the 3D stress state:

$$\mathbf{M} = \begin{bmatrix} \frac{1}{1-d_f} & 0 & 0 & 0 & 0 & 0 \\ 0 & \frac{1}{1-d_m} & 0 & 0 & 0 & 0 \\ 0 & 0 & \frac{1}{1-d_i} & 0 & 0 & 0 \\ 0 & 0 & 0 & \frac{1}{1-d_{s12}} & 0 & 0 \\ 0 & 0 & 0 & 0 & \frac{1}{1-d_{s13}} & 0 \\ 0 & 0 & 0 & 0 & 0 & \frac{1}{1-d_{s23}} \end{bmatrix} \tag{19}$$

where d_f, d_m, and d_i represent damage variables for fiber, matrix, and interlamina failure modes, repetitively. d_{s12}, d_{s13}, and d_{s23} denote three shear damage variables.

Based on the Tsai-Wu criterion, d_f, d_m, and d_i are independent and regulated by the corresponding tension and compression values which will be demoted by subscripts t and s. In addition, shear damage terms are assumed to be dependent on the fiber, matrix, and interlaminar damages. The explicit expressions of damage variables are:

$$\begin{cases} d_f = 1-(1-d_{ft})(1-d_{fc}) \\ d_m = 1-(1-d_{mt})(1-d_{mc}) \\ d_i = 1-(1-d_{it})(1-d_{ic}) \end{cases} \qquad \begin{cases} d_{s12} = 1-(1-d_f)(1-d_m) \\ d_{s13} = 1-(1-d_f)(1-d_i) \\ d_{s23} = 1-(1-d_m)(1-d_i) \end{cases} \tag{20}$$

Considering the damage operator matrix Eq. (19), the damaged compliance matrix can be obtained as:

$$\mathbf{H}^{\mathrm{d}} = \begin{bmatrix} \frac{1}{(1-d_f)E_1} & -\frac{v_{21}}{E_2} & -\frac{v_{31}}{E_3} & 0 & 0 & 0 \\ -\frac{v_{12}}{E_1} & \frac{1}{(1-d_m)E_2} & -\frac{v_{32}}{E_3} & 0 & 0 & 0 \\ -\frac{v_{13}}{E_1} & -\frac{v_{23}}{E_2} & \frac{1}{(1-d_i)E_3} & 0 & 0 & 0 \\ 0 & 0 & 0 & \frac{1}{(1-d_{s12})G_{12}} & 0 & 0 \\ 0 & 0 & 0 & 0 & \frac{1}{(1-d_{s13})G_{13}} & 0 \\ 0 & 0 & 0 & 0 & 0 & \frac{1}{(1-d_{s23})G_{23}} \end{bmatrix} \tag{21}$$

and the corresponding damaged stiffness matrix is obtained by inverting the compliance matrix:

$$\mathbf{C}^{\mathrm{d}} = \frac{1}{\Delta^{\mathrm{d}}} \begin{bmatrix} C_{11}^{\mathrm{d}} & C_{12}^{\mathrm{d}} & C_{13}^{\mathrm{d}} & 0 & 0 & 0 \\ C_{21}^{\mathrm{d}} & C_{22}^{\mathrm{d}} & C_{23}^{\mathrm{d}} & 0 & 0 & 0 \\ C_{31}^{\mathrm{d}} & C_{32}^{\mathrm{d}} & C_{33}^{\mathrm{d}} & 0 & 0 & 0 \\ 0 & 0 & 0 & C_{44}^{\mathrm{d}} & 0 & 0 \\ 0 & 0 & 0 & 0 & C_{55}^{\mathrm{d}} & 0 \\ 0 & 0 & 0 & 0 & 0 & C_{66}^{\mathrm{d}} \end{bmatrix} \tag{22}$$

with

$$\begin{aligned} \Delta^{\mathrm{d}} =& 1 - (1-d_f)(1-d_m)v_{12}v_{21} - (1-d_f)(1-d_i)v_{13}v_{31} - (1-d_m)(1-d_i)v_{23}v_{32} \\ & - 2 \times (1-d_f)(1-d_m)(1-d_i)v_{12}v_{23}v_{31} \end{aligned}$$

$$\begin{cases} C_{11}^{\mathrm{d}} = (1-d_f)E_1\left[1-(1-d_m)(1-d_i)v_{23}v_{32}\right] \\ C_{12}^{\mathrm{d}} = (1-d_f)(1-d_m)E_1\left[v_{21}+(1-d_i)v_{23}v_{31}\right] \\ C_{13}^{\mathrm{d}} = (1-d_f)(1-d_i)E_1\left[v_{31}+(1-d_m)v_{21}v_{32}\right] \end{cases}$$

$$\begin{cases} C_{21}^{\mathrm{d}} = (1-d_f)(1-d_m)E_2\left[v_{12}+(1-d_i)v_{13}v_{32}\right] \\ C_{22}^{\mathrm{d}} = (1-d_m)E_2\left[1-(1-d_f)(1-d_i)v_{13}v_{31}\right] \\ C_{23}^{\mathrm{d}} = (1-d_m)(1-d_i)E_2\left[v_{32}+(1-d_f)v_{12}v_{31}\right] \end{cases}$$

$$\begin{cases} C_{31}^{\mathrm{d}} = (1-d_f)(1-d_i)E_3\left[v_{13}+(1-d_m)v_{12}v_{23}\right] \\ C_{32}^{\mathrm{d}} = (1-d_m)(1-d_i)E_3\left[v_{23}+(1-d_f)v_{13}v_{21}\right] \\ C_{33}^{\mathrm{d}} = (1-d_i)E_3\left[1-(1-d_f)(1-d_m)v_{12}v_{21}\right] \end{cases}$$

$$\begin{cases} C_{44}^{\mathrm{d}} = \Delta(1-d_{s12})G_{12} \\ C_{55}^{\mathrm{d}} = \Delta(1-d_{s13})G_{13} \\ C_{66}^{\mathrm{d}} = \Delta(1-d_{s23})G_{23} \end{cases}$$

where E_1, E_2, E_3, G_{12}, G_{13}, and G_{23} are undamaged material moduli; v_{12}, v_{21}, v_{13}, v_{31}, v_{23}, and v_{32} are undamaged Poisson's ratios.

3.2 Failure initiation criteria

Damage initiation indicates the onset of stiffness degradation at a material point, which depends on the current stress field. The most widely used form of the Tsai-Wu criterion employs a scalar failure surface, $\mathrm{TW}(\hat{\boldsymbol{\sigma}})$, defined in the effective stress space for orthotropic materials:

$$\begin{aligned} \mathrm{TW}(\hat{\boldsymbol{\sigma}}) =& F_{11}\hat{\sigma}_1^2 + F_{22}\hat{\sigma}_2^2 + F_{33}\hat{\sigma}_3^2 + 2F_{23}\hat{\sigma}_2\hat{\sigma}_3 + 2F_{13}\hat{\sigma}_1\hat{\sigma}_3 + 2F_{12}\hat{\sigma}_1\hat{\sigma}_2 + \\ & F_1\hat{\sigma}_1 + F_2\hat{\sigma}_2 + F_3\hat{\sigma}_3 + F_{44}\hat{\tau}_{23}^2 + F_{55}\hat{\tau}_{12}^2 + F_{66}\hat{\tau}_{12}^2 \end{aligned} \tag{23}$$

where F_i and F_{ij} $(i,j = 1,...,6)$ are strength tensors of the second and fourth rank, respectively. Due to the symmetry of orthotropic materials, certain components such as F_4 and F_{45} are expected to vanish. The failure criterion claims that the structure is safe if $\mathrm{TW} < 1$, whereas the critical condition for failure occurs when $\mathrm{TW} = 1$.

F_i and F_{ii} are related to the one-directional engineering strengths, which can be measured experimentally in the laboratory. These components are defined as:

$$F_{11} = \frac{1}{X_t X_c}; \quad F_{22} = \frac{1}{Y_t Y_c}; \quad F_{33} = \frac{1}{Z_t Z_c};$$
$$F_{44} = \frac{1}{S_I^2}; \quad F_{55} = \frac{1}{S_T^2}; \quad F_{66} = \frac{1}{S_L^2} \tag{24}$$

$$F_1 = \frac{1}{X_t} - \frac{1}{X_c}; \quad F_2 = \frac{1}{Y_t} - \frac{1}{Y_c}; \quad F_3 = \frac{1}{Z_t} - \frac{1}{Z_c} \tag{25}$$

where X_t and X_c represent the uniaxial tensile and compressive fiber strengths; Y_t and Y_c correspond to the tensile and compressive matrix strengths; Z_t and Z_c denote the tensile and compressive interlaminar strengths; S_I, S_T, and S_L are the interlaminar shear strength, transverse shear strength, and longitudinal shear strength, respectively.

The determination of the off-diagonal components, F_{ij}, in the Tsai-Wu criterion is challenging. In the original formulation of the Tsai–Wu criterion [1], the failure envelope is constrained to be an ellipsoid, ensuring that it remains closed. This constraint imposes a condition on F_{ij}:

$$F_{ij}^2 < F_{ii} F_{jj} \tag{26}$$

The constraint of Eq. (26) provides a range for F_{ij} rather than a fixed value. Additionally, [1] noted that F_{ij} can be determined under combined stress states, which can be represented as:

$$\begin{aligned} F_{12} &= \frac{1}{2B_{12}^2}(1 - B_{12}(F_1 + F_2) - B_{12}^2(F_{11} + F_{22}) \\ F_{13} &= \frac{1}{2B_{13}^2}(1 - B_{13}(F_1 + F_3) - B_{13}^2(F_{11} + F_{33}) \\ F_{23} &= \frac{1}{2B_{23}^2}(1 - B_{23}(F_2 + F_3) - B_{23}^2(F_{22} + F_{33}) \end{aligned} \tag{27}$$

where B_{ij} corresponds to the tensile bi-stress strength, which requires difficult biaxial stress tests. This term can be estimated using several outputs according to [43]. Eq. (28) from [43], where a lower bound estimate can be obtained using the maximum failure envelope, is employed in this work.

$$\begin{aligned} B_{12} &= \min\left\{\frac{Y_t}{1-\nu_{21}}, \frac{X_t}{1-\nu_{12}}\right\} \\ B_{13} &= \min\left\{\frac{Z_t}{1-\nu_{31}}, \frac{X_t}{1-\nu_{13}}\right\} \\ B_{23} &= \min\left\{\frac{Z_t}{1-\nu_{32}}, \frac{Y_t}{1-\nu_{23}}\right\} \end{aligned} \tag{28}$$

An alternative empirical approach based on the generalization of the von Mises criterion [44, 45] was also proposed, which satisfies the constraint in Eq. (26). This empirical expression is given by:

$$F_{ij} = -\frac{1}{2}\sqrt{F_{ii} F_{jj}} \tag{29}$$

As demonstrated in [46], the assumption of a closed failure envelope is not universally valid for all composites, and the constraint in Eq. (26) may be relaxed under certain circumstances. Nevertheless, for the composites considered in this work, F_{ij} satisfies Eq. (26). Accordingly, F_{ij} is first calculated using Eq. (27). If the computed values violate the condition in Eq. (26), the empirical expression in Eq. (29) is applied instead.

3.3 Damage evolution

Once $\mathrm{TW}(\hat{\boldsymbol{\sigma}}) = 1$, further loading will cause the degradation of material stiffness coefficients. The reduction in stiffness coefficients is governed by damage variables that range from zero for intact material to one for completely damaged material.

In this framework, the evolution laws for each damage variable can be formulated in the strain space, as described in [6]. New variables are introduced based on the definitions of equivalent stresses and strains. These equivalent measures are derived using the generalized equivalent principal virtual work, expressed as:

$$\sigma_{eq}\varepsilon_{eq} = \sum \sigma_{ij}\varepsilon_{ij}, \quad \text{and} \quad \varepsilon_{eq} = \sqrt{\sum \varepsilon_{ij}^2}, \quad i,j = 1,2,...,6 \tag{30}$$

For the specific cases of fiber, matrix, and interlaminar failure, the corresponding equivalent strains and stresses are reformulated:

$$\begin{cases} \varepsilon_{eq,ft} = \sqrt{\langle\varepsilon_1\rangle^2 + \gamma_{12}^2 + \gamma_{13}^2} \\ \varepsilon_{eq,fc} = \langle -\varepsilon_1 \rangle \\ \varepsilon_{eq,mt} = \sqrt{\langle\varepsilon_2\rangle^2 + \langle\varepsilon_3\rangle^2 + \gamma_{21}^2 + \gamma_{23}^2 + \gamma_{31}^2} \\ \varepsilon_{eq,mc} = \sqrt{\langle -\varepsilon_2\rangle^2 + \langle -\varepsilon_3\rangle^2 + \gamma_{21}^2 + \gamma_{23}^2 + \gamma_{31}^2} \\ \varepsilon_{eq,it} = \sqrt{\langle\varepsilon_3\rangle^2 + \gamma_{31}^2 + \gamma_{32}^2} \\ \varepsilon_{eq,ic} = \langle -\varepsilon_3 \rangle \end{cases} \tag{31}$$

$$\begin{cases} \sigma_{eq,ft} = \dfrac{\langle\sigma_1\rangle\langle\varepsilon_1\rangle + \tau_{12}\gamma_{12} + \tau_{13}\gamma_{13}}{\sqrt{\langle\varepsilon_1\rangle^2 + \gamma_{12}^2 + \gamma_{13}^2}} \\ \sigma_{eq,fc} = \langle -\sigma_1 \rangle \\ \sigma_{eq,mt} = \dfrac{\langle\sigma_2\rangle\langle\varepsilon_2\rangle + \langle\sigma_3\rangle\langle\varepsilon_3\rangle + \tau_{21}\gamma_{21} + \tau_{23}\gamma_{23} + \tau_{31}\gamma_{31}}{\sqrt{\langle\varepsilon_2\rangle^2 + \langle\varepsilon_3\rangle^2 + \gamma_{21}^2 + \gamma_{23}^2 + \gamma_{31}^2}} \\ \sigma_{eq,mc} = \dfrac{\langle -\sigma_2\rangle\langle -\varepsilon_2\rangle + \langle -\sigma_3\rangle\langle -\varepsilon_3\rangle + \tau_{21}\gamma_{21} + \tau_{23}\gamma_{23} + \tau_{31}\gamma_{31}}{\sqrt{\langle -\varepsilon_2\rangle^2 + \langle -\varepsilon_3\rangle^2 + \gamma_{21}^2 + \gamma_{23}^2 + \gamma_{31}^2}} \\ \sigma_{eq,it} = \dfrac{\langle\sigma_3\rangle\langle\varepsilon_3\rangle + \tau_{31}\gamma_{31} + \tau_{32}\gamma_{32}}{\sqrt{\langle\varepsilon_3\rangle^2 + \gamma_{31}^2 + \gamma_{32}^2}} \\ \sigma_{eq,ic} = \langle -\sigma_3 \rangle \end{cases} \tag{32}$$

where $< \cdot >$ is the Macaulay bracket to have non negative values.

To define the damage evolution laws, it is necessary to obtain the equivalent stress, $\sigma_{eq,I}^0$, and equivalent strain, $\sigma_{eq,I}^0$, at the onset of damage initiation. In the effective stress space, the effective stress varies linearly with strain. Thus, the following relation is obtained:

$$\hat{\sigma}_{ij}^{\text{onset}} = \beta\hat{\sigma}_{ij}(d_0), \quad \hat{\sigma}_{ij}(d_0) \propto \epsilon_{ij}(d_0) \implies \epsilon_{ij}^{\text{onset}} = \beta\epsilon_{ij}(d_0) \tag{33}$$

where $\hat{\sigma}_{ij}^{\text{onset}}$ denotes the effective stress at the onset of damage, which can be determined by scaling the effective stress $\hat{\sigma}_{ij}(d_0)$ with damage d_0. Similarly, the strain at the onset of damage, $\epsilon_{ij}^{\text{onset}}$, is determined by scaling the strain $\epsilon_{ij}(d_0)$ with damage d_0.

The determination of the scaling factor β involves solving the Tsai–Wu criterion:

$$\mathrm{TW}(\beta\hat{\boldsymbol{\sigma}}) = 1 \tag{34}$$

where TW is defined in Eq. (23). Substituting Eq. (23) into Eq. (34) leads to a quadratic equation for β, as shown below:

$$\begin{aligned}\beta^2 \underbrace{\left(2F_{12}\hat{\sigma}_1\hat{\sigma}_2 + 2F_{13}\hat{\sigma}_1\hat{\sigma}_3 + 2F_{23}\hat{\sigma}_2\hat{\sigma}_3 + F_{11}\hat{\sigma}_1^2 + F_{22}\hat{\sigma}_2^2 + F_{33}\hat{\sigma}_3^2\right.}_{a} \\ \underbrace{\left. + F_{66}\hat{\tau}_{12}^2 + F_{55}\hat{\tau}_{13}^2 + F_{44}\hat{\tau}_{23}^2\right)}_{a} + \beta \underbrace{\left(F_1\hat{\sigma}_1 + F_2\hat{\sigma}_2 + F_3\hat{\sigma}_3\right)}_{b} + \underbrace{(-1)}_{c} = 0\end{aligned} \tag{35}$$

in which a, b, and c are coefficients of the quadratic equation. Therefore, β is given by:

$$\beta = \frac{-b + \sqrt{b^2 - 4ac}}{2a} \tag{36}$$

In many orthotropic damage models, it is assumed that damage evolution primarily depends on the stresses and strains associated with the corresponding damage plane. Therefore, the Tsai–Wu failure criterion must be independently solved for fiber, matrix, and interlaminar behavior under both tension and compression. To ensure consistency, Eq. (35), used to calculate the β variable, must include only the stress components corresponding to the equivalent stresses defined in Eq. (32) for each failure mode I, i.e., fiber, matrix, and interlaminar, in tension and compression.

In this work, the damage evolution laws for each failure mode I are defined based on a linear softening path. To mitigate the mesh dependency, an equivalent displacement-stress relationship, as shown in Fig. 3, is obtained by introducing the characteristic element length l_c. Then, the damage evolution function of each damage variable is expressed as:

$$d_I = \frac{\delta_{eq,I}^u(\delta_{eq,I} - \delta_{eq,I}^0)}{\delta_{eq,I}(\delta_{eq,I}^u - \delta_{eq,I}^0)}, \quad \text{if} \quad \delta_{eq,I}^0 \le \delta_{eq,I} \le \delta_{eq,I}^u \tag{37}$$

with

$$\delta_{eq,I}^0 = l_c\varepsilon_{eq,I}^0 \quad \text{and} \quad \delta_{eq,I}^u = \frac{2G_{\mathrm{f},I}}{\sigma_{eq,I}^0} \tag{38}$$

where $\delta_{eq,I}^0$ and $\sigma_{eq,I}^0$ are the equivalent displacements and stresses, respectively, at the onset of damage. $\delta_{eq,I}^u$ is the ultimate equivalent displacement when the material is fully damaged.

It is evident that l_c directly influences the softening curve by controlling the ultimate equivalent displacement $\delta_{eq,I}^u$. Smaller values of l_c lead to gradual softening curves, while larger values result in steeper softening. This relationship ensures that the total energy dissipation remains consistent with the experimental fracture energy.

3.4 Characteristic element length

Determining the characteristic element length is critical in fracture energy regularization techniques to maintain the objectivity of energy dissipation. This length should reflect the evolving width of the fracture zone throughout the fracture process [47]. Traditional methods that rely solely on constant calculations of element areas or volumes are often insufficient [48]. As highlighted by [49], the determination of l_c depends on several factors, including the

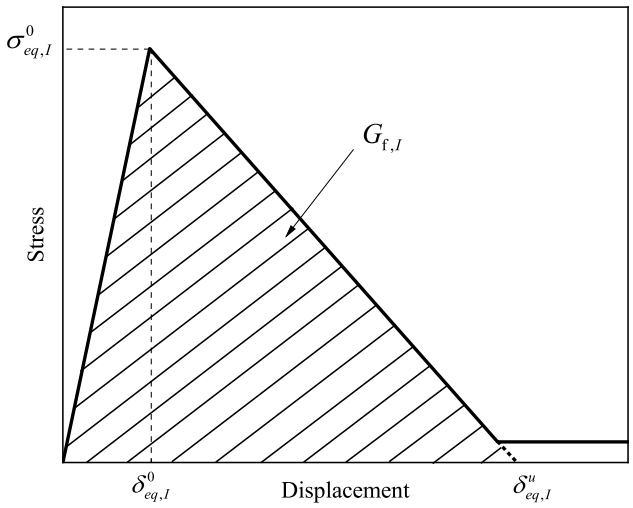

Figure 3: Equivalent displacement-stress for fiber, matrix, and interlamina

shape and size of element, the interpolation function employed, the integration scheme, and the mesh line orientation. This work employs the projection method proposed by [41].

Figure 4 employs a B3 beam element with one L9 expansion element to explain the idea of [41]. First, a volume is constructed using the beam element through Lagrange expansion. Two parameters α_1 and α_2 are introduced to scale the beam element length and cross-sectional dimensions, leading to a scaled sub-volumes. For second-order elements shown in Fig. 4, α_1 and α_2 are set to 0.5 according to [41]. Subsequently, a projection method is applied to the scaled sub-volumes containing the target point, i.e., Gauss point (GP). This projection method determines the l_c along the unit vector of the major principal strain at each GP, indicating each GP from the same element has an individual l_c. Therefore, the formulation for l_c of each GP, $\mathbf{x}$, can be generalized as:

$$l_c(\mathbf{x}) = |\max[\mathbf{x_n} \cdot \mathbf{n}(\mathbf{x})] - \min[\mathbf{x_n} \cdot \mathbf{n}(\mathbf{x})]| \tag{39}$$

where $\mathbf{x}_n$ is the middle point of the edge in a scaled volume that contains the targeted Gaussian point $\mathbf{x}$, as illustrated in Fig. 4. $\mathbf{n}(\mathbf{x})$ is the unit vector in the major principal strain direction.

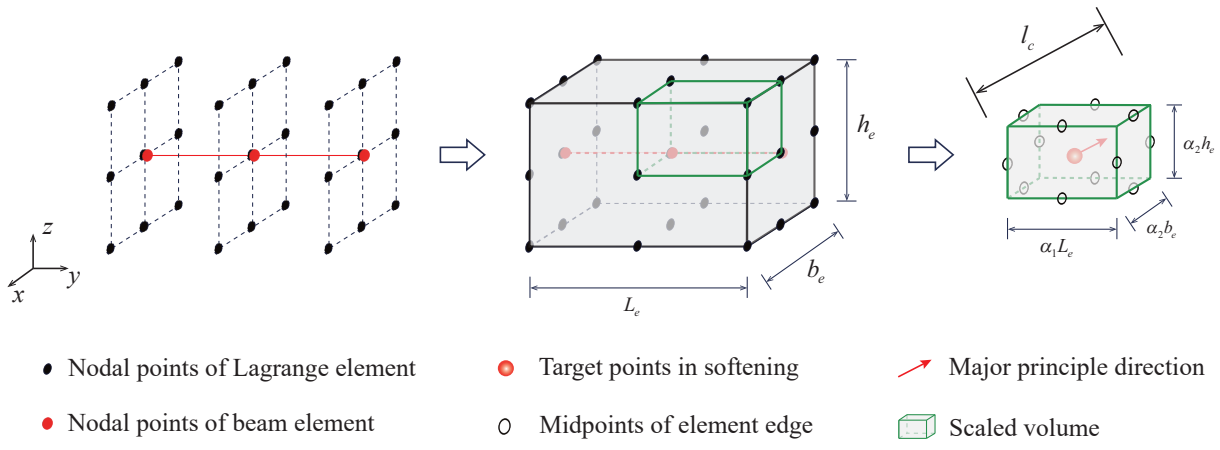

Figure 4: Illustration of calculation for l_c

3.5 Viscous regularization

Although the fracture energy regularization ensures consistent fracture energy dissipation, the governing equations remain ill-posed, highlighting that fracture energy regularization is only a partial regularization technique. This issue can result in the loss of positive definiteness of the tangent stiffness matrix and numerical convergence difficulties.

Therefore, a viscous regularization scheme can be implemented directly to mitigate these numerical issues. This approach relies on the artificial Duvaut-Lions viscosity model, which ensures that the tangent stiffness matrix of softening materials remains positive definite for sufficiently small time increments.

In damage modeling, the viscous damage variable in the regularization scheme is defined as follows:

$$\delta d_I^v = \frac{1}{\eta_I}(d_I - d_I^v) \times \delta_t \tag{40}$$

where η_I represents a viscosity coefficient indicating the relaxation time of the viscous system, d_I means the non-viscous damage variable and d_I^v denotes viscous damage variable corresponding to mode I (including various concrete and composite damage modes). The damaged material response is then evaluated using the viscous damage variables.

A numerical algorithm is required to solve Eq. (40). A straightforward approach is to update the viscous damage variable using the backward Euler method, expressed as:

$$d_I^v(t_0 + \Delta t) = \frac{\Delta t}{\eta + \Delta t} d_I^v(t_0 + \Delta t) + \frac{\eta}{\eta + \Delta t} d_I^v(t_0) \tag{41}$$

where Δt is size of time step.

Eq. (41) indicates the current viscous damage variable $d_I^v(t_0 + \Delta t)$ is determined as a weighted combination of the current non-viscous damage variable $d_I^v(t_0+\Delta t)$ and the previous viscous damage variable $d_I^v(t_0)$.

4 Numerical examples

This section investigates the progressive damage behavior of three pultruded composite structures using the proposed numerical models. For all numerical tests, the displacement control method was employed. The load-displacement responses and damage patterns were obtained and compared to the experimental data.

4.1 Compact tension test

The first example is based on an orthotropic Glass Fiber Reinforced Polymer (GFRP) specimen which was conducted experimentally in the work of [50] to assess the fracture energy through a Compact Tension (CT) test. The full details of the experimental layout is shown in Fig. 5(a). The loading and geometrical conditions of the CT specimen are illustrated in Fig. 5(b). The specimen has a thickness of 10 mm, with the lower pin clamped and a vertical displacement applied to the upper pin until a maximum value of 1.2 mm is reached. The material properties relevant to the strength and fracture energies of the GFRP material are summarized in Table 1.

Beam elements can be assigned along the thickness of the specimen which is shown in Fig. 6(a). The cross-sectional discretization is illustrated in Fig. 6(b), where Lagrange elements are employed. In this cross-section, the fiber direction is oriented along the z-axis, and the

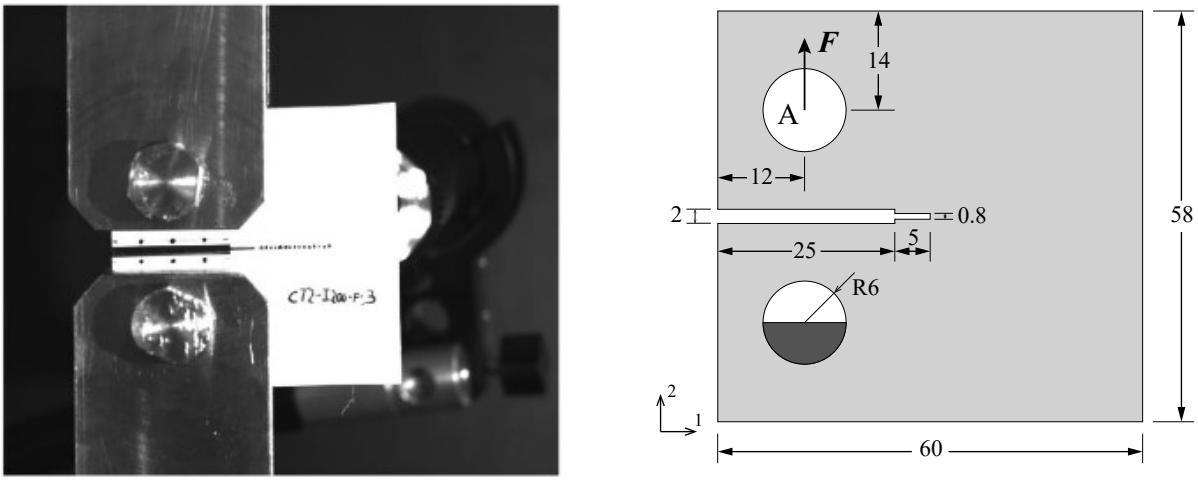

(a) (b)

Figure 5: (a) Experimental layout [50] and (b) geometry for CT test (mm)

Table 1: Material properties of the notched GFRP specimen

Properties	Units	Symbols	Values	Symbols	Values
Elastic moduli	GPa	E_{11}	30	G_{12}	3.0
		E_{22}	12	G_{13}	3.0
		E_{33}	12	G_{23}	3.0
Poisson's ratios	-	v_{12}	0.24		
		v_{13}	0.24		
		v_{23}	0.3		
Strengths	MPa	X_t	323	X_c	426
		Y_t	71	Y_c	71
		Z_t	71	Z_c	71
		S_L	67	S_T	64
		S_I	64		
Fracture energies	MPa·mm	G_{ft}	100	G_{fc}	100
		G_{mt}	20	G_{mc}	20
		G_{it}	20	G_{ic}	20

matrix is aligned along the x-axis. The gray circular supports in Fig. 6(b) are modeled with a linear isotropic steel material.

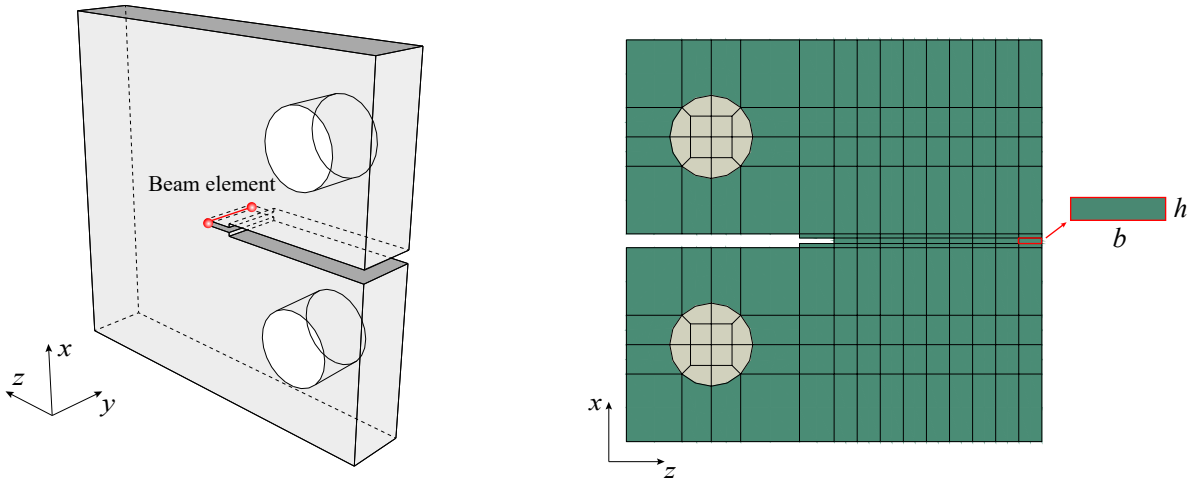

(a) (b)

Figure 6: (a) Beam elements and (b) cross-sectional discretizations of the CT specimen

To fully validate the proposed fracture energy regularization technique for mitigating mesh dependency, Table 2 lists ten CUF-based beam models. These models account for variations in both the size and order of beam elements as well as the cross-sectional discretization, i.e., structural theory. The meaning of 'b' and 'h' in Table 2 can be seen in Fig. 6(b).

Table 2: Model information for CT test

Model No.	Cross-sectional discretization		Beam discretization		DOF
	Number	b×h (mm×mm)[1]	Number	Length (mm)[2]	
Model 1	157 L4	3.33×0.8	1 B2	10	1,332
Model 2	157 L4	3.33×0.8	1 B3	10	1,896
Model 3	157 L4	3.33×0.8	1 B4	10	2,460
Model 4	157 L9	3.33×0.8	1 B4	10	8,925
Model 5	157 L16	3.33×0.8	1 B4	10	19,500
Model 6	175 L4	3.33×0.267	1 B4	10	2,700
Model 7	388 L4	1.0×0.8	1 B4	10	5,484
Model 8	388 L16	1.0×0.8	1 B4	10	44,916
Model 9	388 L16	1.0×0.8	2 B4	5	77,730
Model 10	388 L16	1.0×0.8	3 B4	3.33	110,544

[1] The individual discretized cross-sectional mesh size in the notch.
[2] The individual beam element length.

The load-displacement diagrams of all numerical models are plotted in Fig. 7, including experimental results for comparison. In Fig. 7(a), Models 1 to 3, which vary in beam element order, show nearly identical curves, suggesting that the beam element order has minimal impact on numerical results in this case. However, with higher-order LE, as seen in Models 4 and 5, the initial stiffness and post-peak softening responses are slightly reduced compared to the first three models. This minor variation can be attributed to the improved capability of higher-order LE to capture cross-sectional deformation. Overall, the numerical results closely

align with the experimental data in Fig. 7(a), confirming that the proposed model effectively mitigates the influence of beam element and cross-sectional LE order.

In Fig. 7(b), Models 3, 6, and 7 explore the influence of LE size by varying the number of LE, while Models 8 to 10 examine the influence of beam element size by adjusting the number of beam elements along the thickness. The curves in Fig. 7(b) can be separated into two distinct groups: one group with L4 models and the other with L16 models. Within each group, the curves are nearly coincident and within the experimental ranges, indicating the proposed method effectively achieves mesh size independence. However, L4 models yield slightly higher curves than L16 models, likely due to the linear approximation in L4 models compared to the higher-order approximation in L16 models. This distinction highlights the enhanced accuracy of L16 models in capturing the structural response.

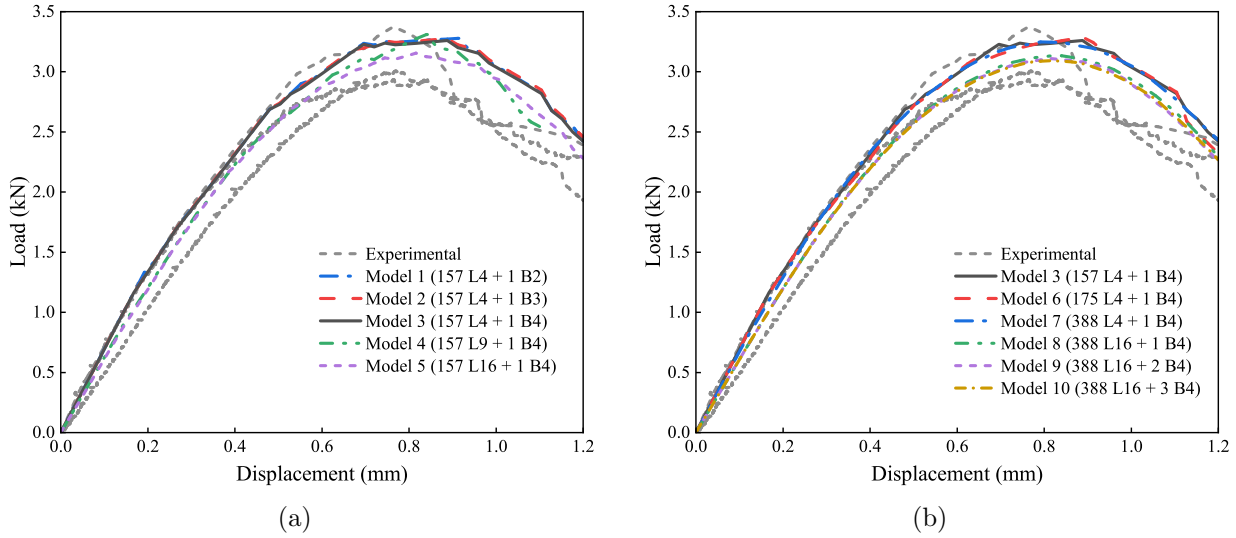

Figure 7: Reaction load-displacement curves of the CT test from various CUF-based models: (a) Influence of order and (b) influence of mesh size

Since external loads are applied along the x-axis, aligned with the direction of the matrix, Fig. 8 shows the progression of the tensile and compressive damage within the matrix in the CT test of Model 5. The results indicate that the damage begins at the corner of the notch and propagates into the specimen as a narrow band. Compressive matrix damage occurs on the right side of the notch, indicating that it can also be captured in the proposed damage model framework. The applied displacement of 0.816 mm corresponds to the peak load in the load-displacement diagram. Compared to the damage distribution at 1.2 mm displacement, the matrix tensile damage at the peak load appears to have only propagated halfway. Meanwhile, the matrix compressive damage seems to be in its early stages, with only minimal areas showing signs of damage. This phenomenon suggests that satisfying the Tsai-Wu criterion does not necessarily imply the complete failure of the structure. Furthermore, even when the structure reaches its maximum load-carrying capacity, it does not entirely fail and retains some residual loading capacity.

The tensile and compressive matrix damage distributions from other models are similar as those presented in Fig. 8. Although six damage parameters, which are fiber, matrix, and interlaminar damage under compression and tension, are considered in the proposed orthotropic damage models, some of them are almost negligible in this case and will not be presented here.

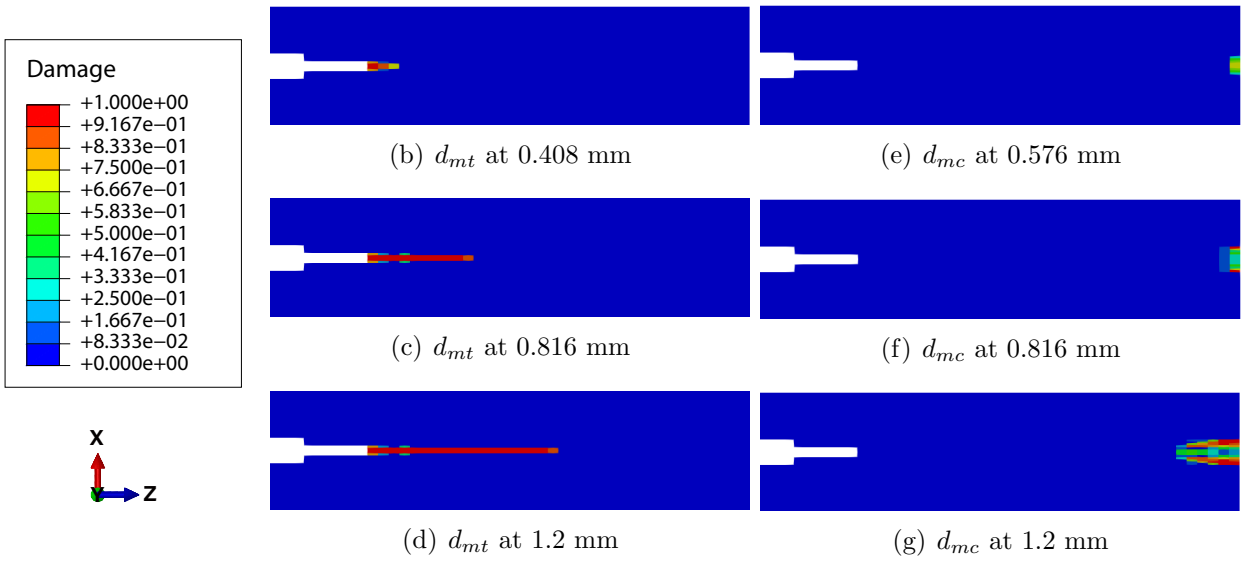

(b) d_{mt} at 0.408 mm (e) d_{mc} at 0.576 mm

(c) d_{mt} at 0.816 mm (f) d_{mc} at 0.816 mm

(d) d_{mt} at 1.2 mm (g) d_{mc} at 1.2 mm

Figure 8: Tensile and compressive matrix damage propagations of the CT test from Model 5

4.2 Three-point bending beam

The pultruded GFRP beam with a notch at mid-span in a Three-Point Bending (TPB) test was investigated originally by [51], in which the mode I fracture properties of pultruded GFRP composites along the matrix direction were extracted. The dimension and loading layout can be seen in Fig. 9. In this case, the loading is controlled by displacement with the maximum value of 1.2 mm and the Crack Mouth Opening Displacements (CMOD) at the notch bottom are obtained for plotting the load-CMOD curves. Based on the work of [27], material properties are summarized in Table 3. The measured fracture energies from [51] and [27] are different. In this work, the average values are employed.

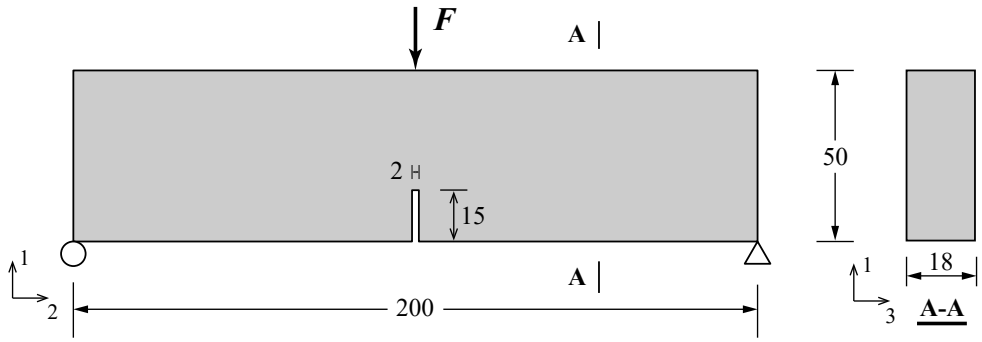

Figure 9: Load and geometry of the TPB beam (mm)

To reduce computational costs, a quarter structure is employed for numerical analysis, which can be seen in Fig. 10. The beam elements are assigned as shown in Fig. 10(a), where only half length of the beam is employed. Six B4 elements are adopted for the un-notched part. Different order and number of beam elements are only employed for the middle notch to investigate the mesh dependency. Five beam element assignments in the notch are shown in Fig. 10(a). The cross-section is halved and discretized as show in Fig. 10(b). Different cross-sectional discretizations are taken into account. Overall, seven CUF models are considered, as detailed in Table 4, in which beam element size and order as well as cross-sectional discretizations are considered.

Table 3: Material properties of the TPB specimen

Properties	Units	Symbols	Values	Symbols	Values
Elastic moduli	GPa	E_{11}	30	G_{12}	2.0
		E_{22}	10.8	G_{13}	2.0
		E_{33}	10.8	G_{23}	2.0
Poisson's ratios	-	v_{12}	0.24		
		v_{13}	0.24		
		v_{23}	0.4		
Strengths	MPa	X_t	323	X_c	423
		Y_t	37	Y_c	80
		Z_t	37	Z_c	80
		S_L	33	S_T	33
		S_I	33		
Fracture energies	MPa·mm	G_{ft}	130	G_{fc}	130
		G_{mt}	5.12	G_{mc}	5.12
		G_{it}	5.12	G_{ic}	5.12

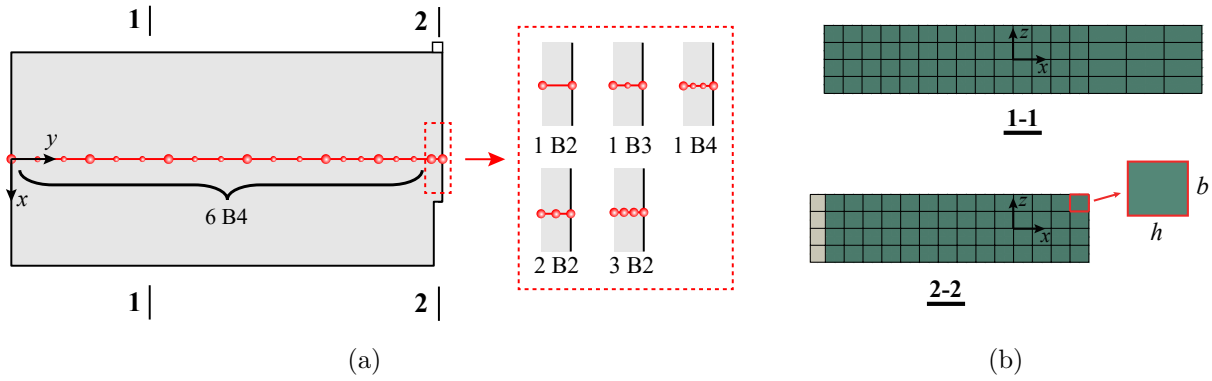

(a) (b)

Figure 10: (a) Beam element and (b) cross-sectional discretizations of the TPB beam

Table 4: Model information for TPB beam

Model No.	Cross-sectional discretization		Beam discretization		DOF
	Number[1]	b×h (mm×mm)	Number	Length (mm)[2]	
Model 1	45 L9	3.00×2.92	6 B4 + 1 B2	1.00	12,978
Model 2	45 L9	3.00×2.92	6 B4 + 1 B3	1.00	13,545
Model 3	45 L9	3.00×2.92	6 B4 + 1 B4	1.00	14,112
Model 4	68 L9	2.25×2.50	6 B4 + 1 B2	1.00	18,846
Model 5	80 L9	2.25×2.06	6 B4 + 1 B2	1.00	22,086
Model 6	80 L9	2.25×2.06	6 B4 + 2 B2	0.50	23,085
Model 7	80 L9	2.25×2.06	6 B4 + 3 B2	0.33	24,084

[1] The number of L9 in Section 1-1 shown in Fig. 10(b).
[2] The individual beam element length in the notch.

Figure 11 shows the vertical reaction load-CMOD curves of seven CUF models, including experimental results from [51] for comparison. For the linear part or before the crack load, all numerical results are close to the experimental results. From Models 1 to 3, it is evident that the use of higher-order beam elements in the notch causes the decrease of peak load, which can be attributed to mesh sensitivity to the element order. The curves of Models 1, 4 and 5 are close with each other, indicating the cross-sectional discretization influence the results significantly. When increasing the number of B2 elements in the notch, Models 6 and 7 present slightly lower curves than Model 5, which can be attributed to the better convergence. However, Models 6 and 7 are close to each other, indicating no mesh dependency.

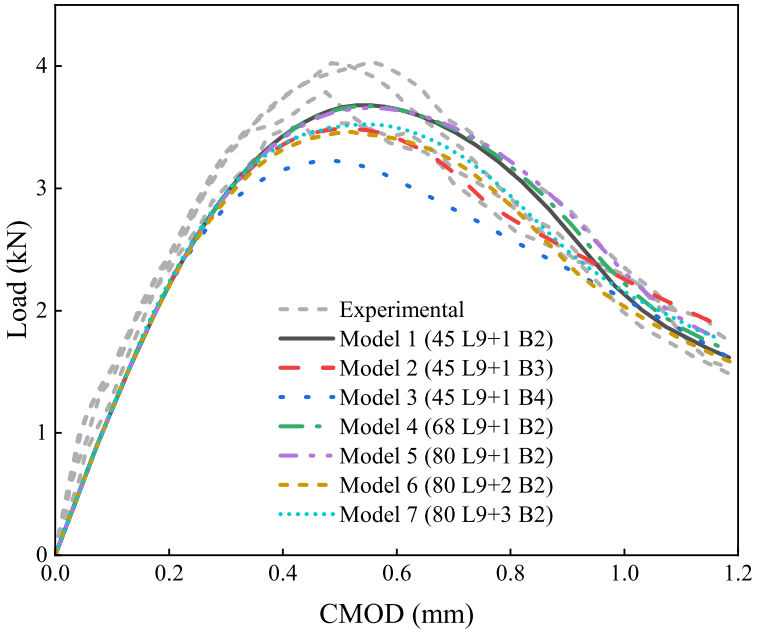

Figure 11: Load-CMOD curves of the TPB beam across different CUF models

Under TPB loading, the matrix, aligned along the y-axis, exhibits significant damage compared to other damage variables. Figure 12 shows that all models exhibit a distinct and narrow tensile damage band in the midspan notched section. Meanwhile, Figure 13 displays that all models exhibit a slightly compressive damage near the loading plate. These consistent matrix damage distributions across all models demonstrate the accuracy of proposed numerical models.

The most efficient model in Table 4 is Model 1 which requires 12,978 DOF. Since the critical zone of this structure is the notched part in the middle which is small compared to the whole structure, it is possible to apply the NDK approach to enhance the efficiency of the CUF model. Based on the Model 1, three NDK models are shown in Fig. 14. In NDK 1, beam nodes in two B4 elements close to the notch employ LE, while the rest employ TE. In Fig. 14(b), the zone using LE is further reduced to save more computational costs. The zone using LE in NDK 3 is the same as that in NDK 2. However, some beam nodes using TE3 are adopted between LE and TE1, which can work as a transition.

Based on the three NDK configurations, Table 5 lists five NDK models used in this study. These NDK models are based on Model 1 which adopts seven beam elements and twenty beam nodes. Additionally, the cross-sectional discretization of Model 1 is retained in all NDK models. Models 8 and 9 utilize the NDK 1. However, Models 8 and 9 employ the TE1 and TE3 in non-critical zones, respectively, to evaluate the impact of higher-order TE on structural accuracy. Similarly, Models 10 and 11 are based on NDK 2 and the effects of TE

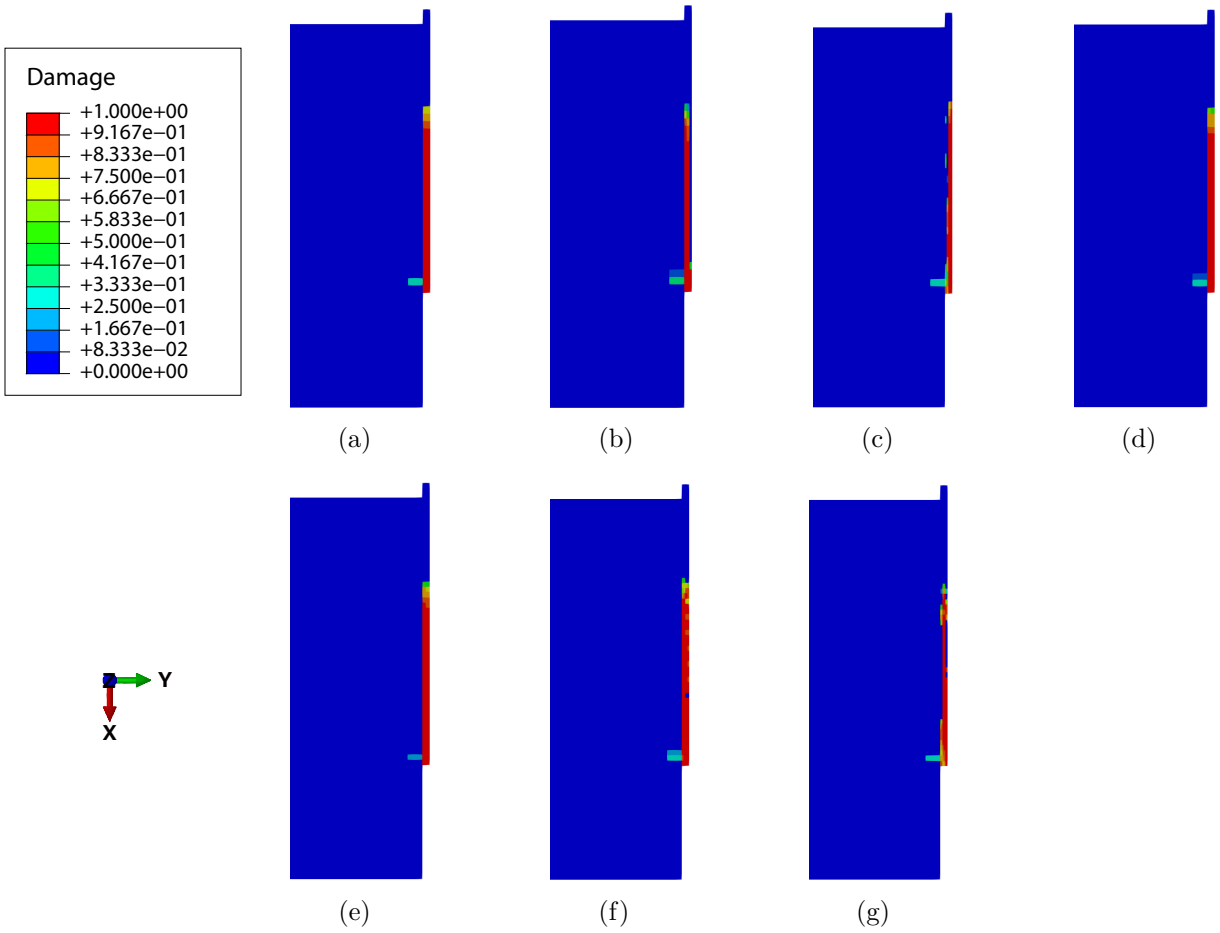

Figure 12: Matrix tensile damage distribution of the TPB beam from (a) Model 1; (b) Model 2; (c) Model 3; (d) Model 4; (e) Model 5; (f) Model 6; (g) Model 7.

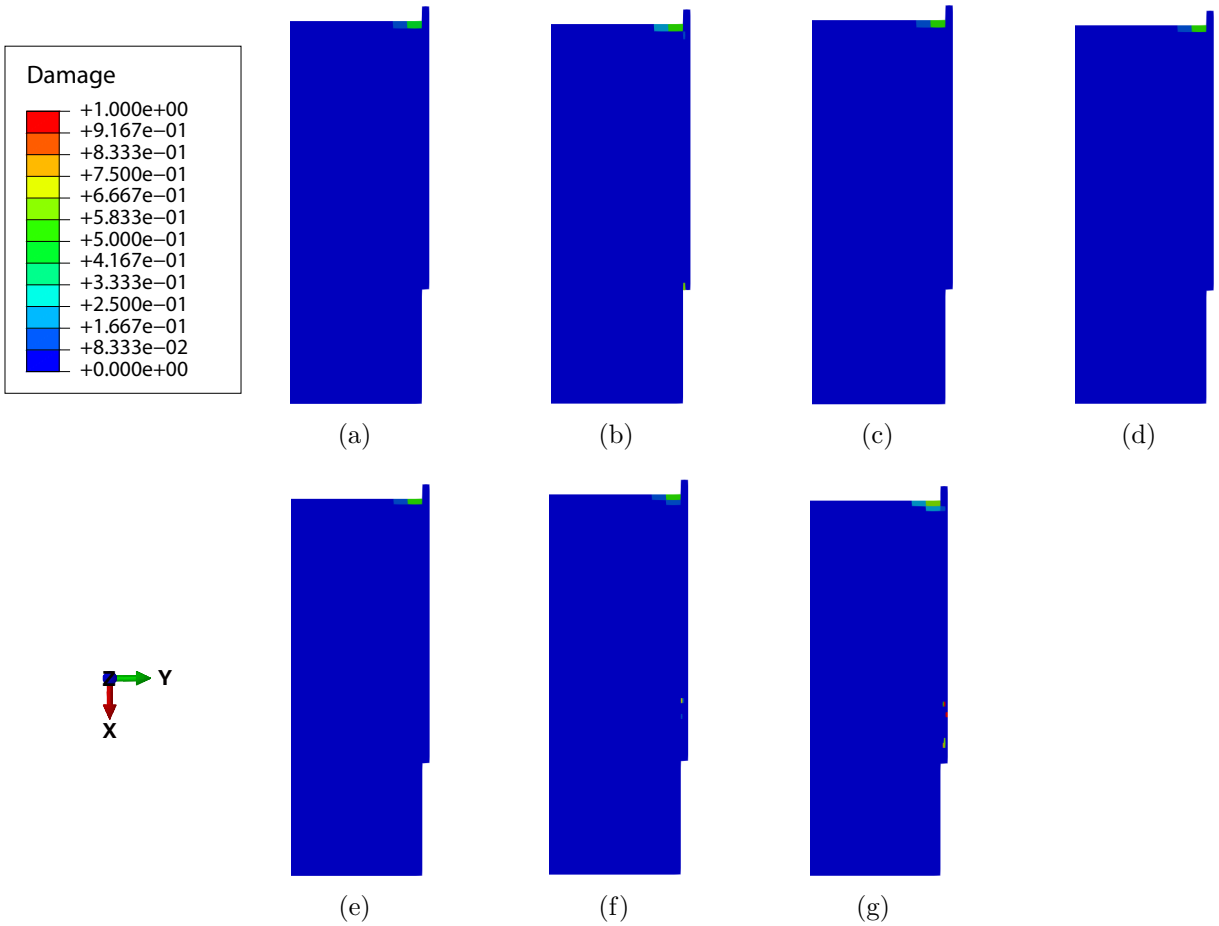

Figure 13: Matrix compressive damage distribution of the TPB beam from (a) Model 1; (b) Model 2; (c) Model 3; (d) Model 4; (e) Model 5; (f) Model 6; (g) Model 7.

orders are investigated. Moreover, Model 12 adopts the NDK 3, where TE3 elements form a transition zone between LE and TE1.

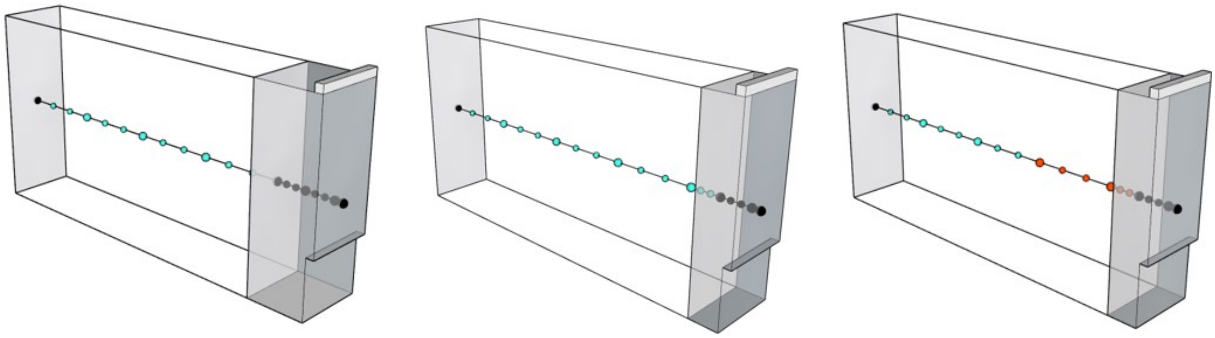

(a) (b) (c)

Figure 14: (a) NDK 1 model, (b) NDK 2 model, and (c) NDK 3 model based on Model 1 for the analysis of the TPB beam-Cyan represents TE1 and red denotes TE3

Table 5: NDK models based on Model 1 for the notched TPB beam

Model No.	NDK type[1]	Expansion of beam nodes[2]	DOF
Model 8	NDK 1	9 LE + 11 TE1	5,916
Model 9	NDK 1	9 LE + 11 TE3	6,147
Model 10	NDK 2	6 LE + 14 TE1	3,390
Model 11	NDK 2	6 LE + 14 TE3	4,284
Model 12	NDK 3	6 LE + 8 TE1 + 6 TE3	4,116

[1] See Fig. 14.
[2] Each model includes 20 beam nodes in total.

The load-CMOD curves of five NDK models are shown in Fig. 15, in which results from the experimental campaign and Model 1 are included for comparison. It is evident that all NDK models cause a higher initial stiffness than Model 1, especially for Model 10 whose curve is out of the experimental range. This phenomenon is expected, as using lower-order kinematics in non-critical zones leads to stiffer numerical models compared to those using higher-order kinematics. Among the NDK models, Model 9 presents the closest curve to the Model 1, as it retains a relatively larger region using LE and the use of TE3 in non-critical zones. In contrast, Model 8, also using the NDK1 but with TE1 in non-critical zones, displays a higher initial stiffness and peak load. For models employing NDK 2, Model 11 closely matches experimental results, while Model 10 provides an incorrect curve outside the experimental range. The accuracy of Model 11 is due to the use of TE3 in non-critical zones. This outcome indicates that higher-order TE in non-critical zones can enhance numerical accuracy when the critical zone is too small. In addition, Model 12 performs similarly to Model 11, but it requires slightly less DOF. These results highlight that the introduction of transition zones using higher-order TE is beneficial for minimizing the required DOF. Except Model 10, all NDK models present structural curves that fall within the experimental range. Moreover, it is worth noting that all NDK models present similar softening curves to Model 1, indicating the the importance of accurately defining the critical zones.

The matrix damage patterns from various NDK models are presented in Figs. 16 and 17. Model 10 exhibits notable deviations, with additional matrix tensile damage appearing

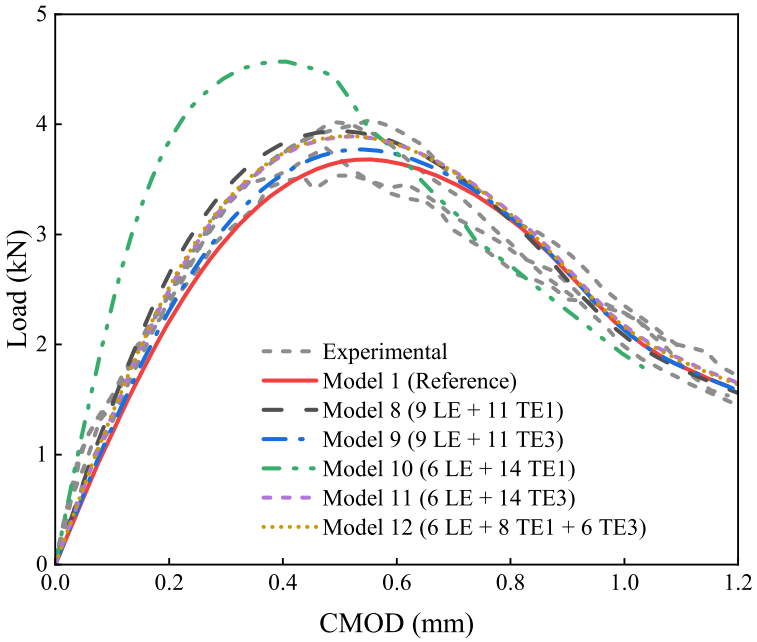

Figure 15: Load-CMOD curves of different NDK models for the TPB beam

outside the notch and more pronounced matrix compressive damage near the loading plate. In contrast, the remaining models display consistent matrix damage patterns, closely aligning with those of Model 1. This consistency suggests that, except for Model 10, all other NDK models effectively replicate the matrix damage behavior observed in the refined model.

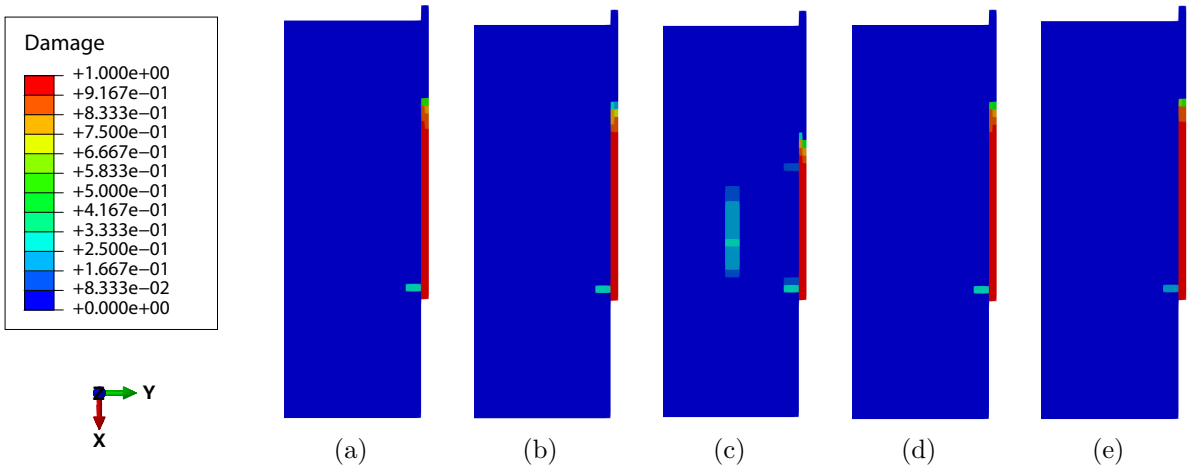

Figure 16: Matrix tensile damage distribution of the TPB beam from (a) Model 8; (b) Model 9; (c) Model 10; (d) Model 11; (e) Model 12.

4.3 Four-point bending test

The final test involves simulating the collapse of a pultruded GFRP beam under Four-Point Bending (FPB) conditions. The experimental campaign of this GFRP beam under FPB test is a part of a large R&D project named CLICKHOUSE [52] and was studied numerically in [53]. The beam is simply supported over a span of approximately 3000 mm and subjected to two-point loading in a classic FPB configuration, as illustrated in Fig. 18. The loads are

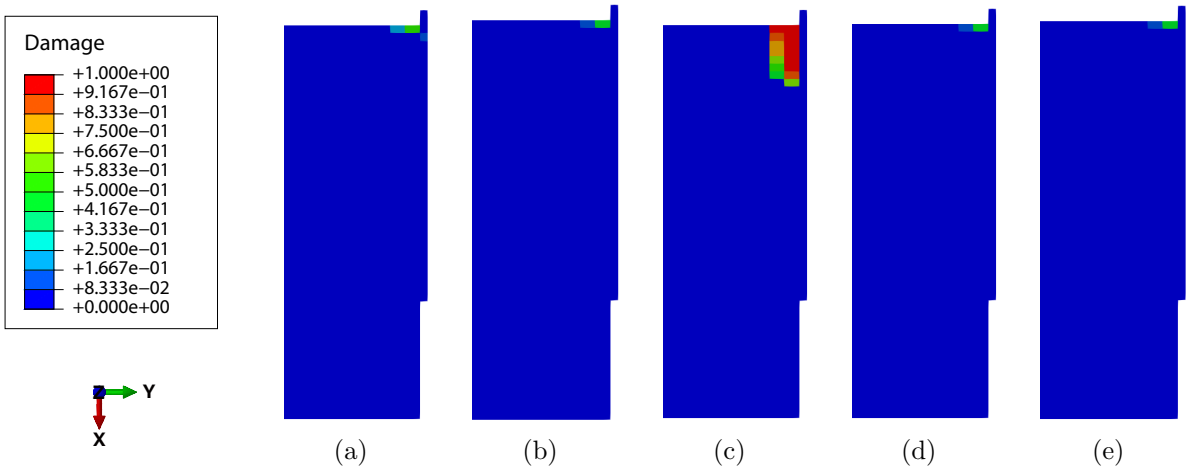

Figure 17: Matrix compressive damage distribution of the TPB beam from (a) Model 8; (b) Model 9; (c) Model 10; (d) Model 11; (e) Model 12.

symmetrically applied at approximately one-third of the span length. The cross-section of the beam is a hollow square profile with an external side length of 120 mm and a thickness of 10 mm. Material properties used for the GFRP composite are obtained from [53] and summarized in Table 6.

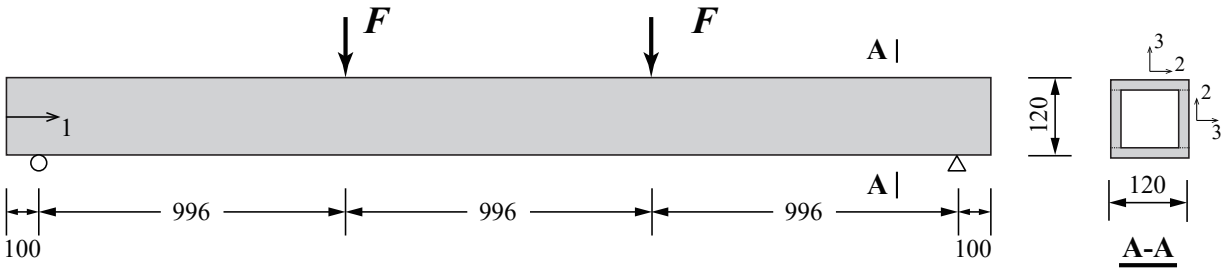

Figure 18: Loads and geometry of the FPB beam (mm)

A half-model of the structure is utilized for numerical analysis to reduce computational costs. Figure 19(a) illustrates the uniform assignment of beam elements. The length of each beam element is approximately 50 mm, which results in a total of 36 beam elements. If the beam element length is reduced to around 30 mm, 56 beam elements will be needed. Three types of cross-sectional discretizations are shown in Fig. 19(b) in which L9 elements are employed with a mesh size of 10 mm.

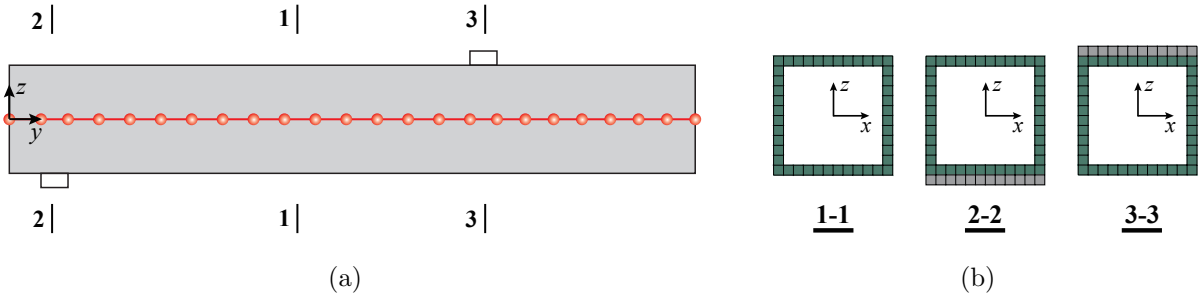

Figure 19: (a) Beam element and (b) cross-sectional discretizations of the FPB beam

Table 6: Material properties of the FPB beam

Properties	Units	Symbols	Values	Symbols	Values
Elastic moduli	GPa	E_{11}	32.4	G_{12}	3.2
		E_{22}	4.8	G_{13}	3.2
		E_{33}	4.8	G_{23}	3.2
Poisson's ratios	-	v_{12}	0.3		
		v_{13}	0.3		
		v_{23}	0.3		
Strengths	MPa	X_t	326.2	X_c	326.2
		Y_t	88.9	Y_c	88.9
		Z_t	88.9	Z_c	88.9
		S_L	41.4	S_T	58.7
		S_I	41.4		
Fracture energies	MPa·mm	G_{ft}	55	G_{fc}	95
		G_{mt}	11.5	G_{mc}	11.5
		G_{it}	11.5	G_{ic}	11.5

Eight CUF-based models, detailed in Table 7, are investigated, each employing the identical cross-sectional discretizations. The first four models utilize LE across the entire structure. The key differences among these models are the order and number of beam elements used, aimed at evaluating the regularization technique. Models 5 and 6, based on Model 1, aim to reduce computational costs through the NDK approach. Figure 20 illustrates two NDK configurations. The NDK 1 model adopts a conservative strategy, with a relatively small non-critical zone employing TE1 models. In contrast, the NDK 2 model introduces a transition zone employing TE3 models to achieve at least 50 % reduction in DOF. Similarly, Models 7 and 8 apply the NDK strategy based on Model 2 to assess the efficiency of NDK in higher-order beam models. For comparison, a 3D model based on ABAQUS, referred to as the ABQ 3D model, is also included. This model uses C3D8 solid elements with an approximate element size of 10 mm. The same damage model is implemented in the ABQ 3D model using the UMAT subroutine.

Table 7: Model information the GFRP beam for the FPB test

Model No.	Model type	Beam elements	Size (mm)[1]	DOF
Model 1	Full LE	36 B2	50	30,204
Model 2	Full LE	36 B3	50	59,316
Model 3	Full LE	36 B4	50	88,428
Model 4	Full LE	56 B2	30	46,044
Model 5	NDK 1	36 B2	50	19,725
Model 6	NDK 2	36 B2	50	15,153
Model 7	NDK 1	36 B3	50	37,375
Model 8	NDK 2	36 B3	50	29,955
ABQ 3D	-	-	-	42,972

[1] Individual beam element length.

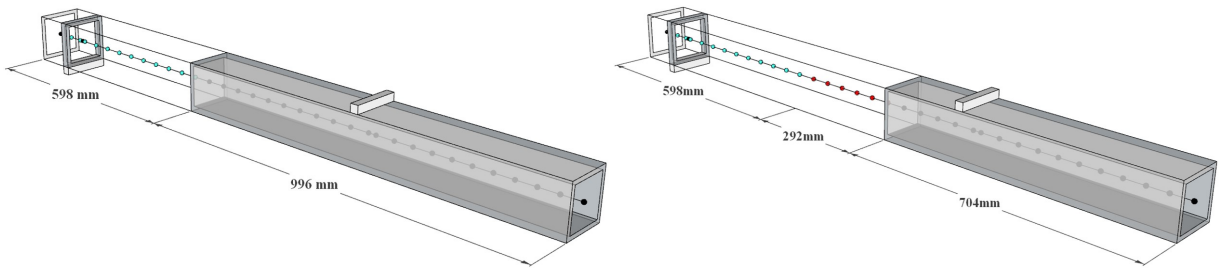

(a) (b)

Figure 20: (a) NDK 1 model and (b) NDK 2 model for the FPB beam-Black represents LE, cyan stands for TE1, and red denotes TE3

The load-displacement curves in Fig. 21 provide a detailed comparison of different numerical models applied to the FPB beam under bending. The experimental data from [53] reported a peak load of approximately 81 kN, serving as a reference for validation. Figure 21(a) highlights the results from various refined beam models with different beam element configurations. Figure 21(b) compares the refined models with their corresponding NDK models to evaluate the accuracy of the NDK approach. Overall, all numerical models, including the CUF-based models and the ABQ 3D model, effectively capture the brittle failure behavior of the FPB beam, which is characterized by a linear elastic phase followed by a rapid loss of load-bearing capacity after reaching the peak load. In the elastic phase, all models exhibit consistent load-displacement curves with minimal variations in stiffness. Although the NDK models show slightly higher stiffness compared to the refined models, this difference is not pronounced in the plotted curves due to the conservative selection of non-critical zones. The alignment between the CUF-based models and the ABQ 3D results further proves the accuracy of the CUF framework in capturing the elastic response of the FPB beam. At the peak load, all models predict slightly higher values than the experimental peak load of 81 kN. This consistent results across different CUF-based models demonstrates their ability to capture the ultimate load capacity. Additionally, their close agreement with the ABQ 3D model confirms the accuracy of the CUF-based framework.

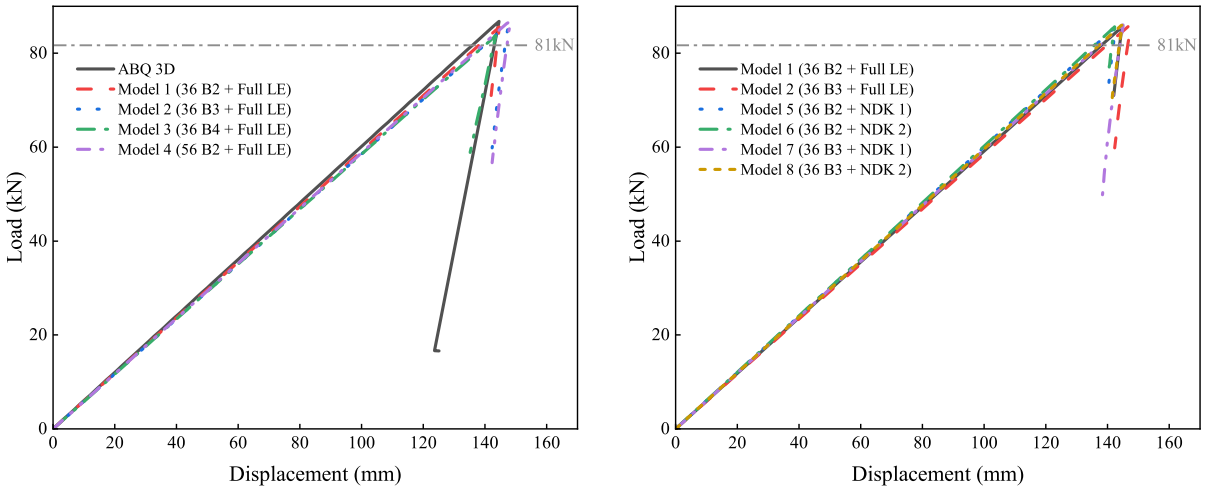

(a) (b)

Figure 21: Load–displacement curves of the FPB beam at mid-span from various numerical models

To further assess model performance, Table 8 summarizes the peak loads and corresponding displacements for each model. Excluding Model 3, the other refined models estimate a peak load of approximately 86 kN, representing a minor overestimation of about 6% compared to the experimental data. The results from the refined models closely align with those of the ABQ 3D model, indicating that mesh dependency has been mitigated to a significant extent. Moreover, all NDK models predict peak loads around 86 kN, which closely match their refined counterparts. However, Models 5 and 6 show slightly lower displacements at peak loads than Model 1. This small difference is likely due to the stiffer response of the NDK models caused by using lower-order kinematics in non-critical regions. A similar pattern is seen in Models 2, 7, and 8. Nevertheless, these differences are minor, confirming the accuracy of the NDK models.

Table 8: Peak results of the FPB GFRP beam from various models and experiment

Model No.	Model type	Peak load (kN)	Displacement (mm) [1]
Exp [53]	-	81.0	-
Model 1	36 B2 + Full LE	85.57	144.65
Model 2	36 B3 + Full LE	86.02	147.34
Model 3	36 B4 + Full LE	83.66	143.50
Model 4	56 B2 + Full LE	86.85	148.29
Model 5	36 B2 + NDK 1	85.58	142.53
Model 6	36 B2 + NDK 2	85.59	142.24
Model 7	36 B3 + NDK 1	85.93	145.07
Model 8	36 B3 + NDK 2	86.08	144.81
ABQ 3D	-	85.61	146.84

[1] It indicates the displacement corresponding to the peak load.

As shown in Fig. 22, experimental failure occurred at the intersection of the top flange with the webs, starting near the load application points, from which the fractures developed and propagated. Additionally, crack is also evident at the junction of the web and flange at the bottom of the beam beneath the right loading point. This kind of failure is attributed to the weaker material properties of web-flange junctions in the pultruded GFRP beams. Therefore, shear damage has been identified as the primary failure mechanism in this pultruded GFRP beam [53].

Figure 23 presents the shear damage patterns predicted by all numerical models. Significant damage localization near the right-side loading plate is observed across all models, which is similar to the experimental cracks. Model 3 additionally shows pronounced damage localization near the left-side loading plate, which explains its slightly lower peak load. While Models 2 through 4 do not capture damage at the bottom junction of the flange and web, as seen in Model 1, they accurately predict similar damage patterns at the top junction of the flange and web near the loading plate, which is the primary damage characteristic for this beam. Models 5 and 6, using the NDK approach based on Model 1, do not show damage at the bottom junction of the flange and web. However, they capture the key damage patterns at the top flange-web junction near the loading plate. Similar observations are noted for Models 2, 7, and 8, which utilize B3 beam elements. Model 7 shows some damage at the bottom flange-web junction, while Model 8 does not. Despite these differences, both models effectively capture the critical damage patterns at the top flange-web junction near the loading plate. The ABQ 3D model provides a clear depiction of damage, showing localization

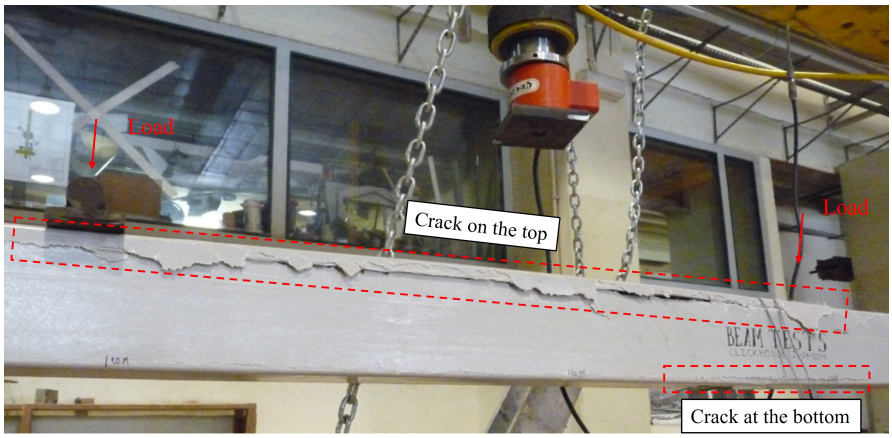

Figure 22: Experimental failure mode of the FPB beam [53]

below the loading plate and horizontal propagation along both the top and bottom flange-web junctions. The occurrence of damage at the bottom junction in some models, including the ABQ 3D model, is likely due to their convergence at lower post-peak residual loads, whereas certain CUF-based models experience convergence challenges at higher residual loads.

In summary, both the CUF-based models and the ABQ 3D model successfully reproduce the essential damage patterns observed in the experimental benchmark, which are similar to numerical results from [53] using the classical Hashin failure criteria.

5 Conclusions

This work has presented a comprehensive numerical investigation of the progressive damage analysis of pultruded composite structures. A novel 3D orthotropic damage model was integrated into one-dimensional CUF-based beam models, where regularization techniques were applied to mitigate mesh dependency. The NDK approach was also employed to improve the computational efficiency of the CUF-based beam models. The proposed framework was validated through three experimental benchmark tests: compact tension, three-point bending, and four-point bending. Based on the comparison of numerical and experimental results, the following conclusions are drawn:

1) CUF-based beam models with the 3D Tsai-Wu orthotropic damage model can effectively provided numerical progressive damage results, closely matching with experimental data. Notably, Model 1 in the CT test required only 1,332 DOF to achieve 3D-level accuracy, highlighting the computational efficiency of CUF-based beam models.

2) Despite minor mesh order sensitivity, most refined CUF-based models consistently produced accurate results. These consistencies confirmed the effectiveness of proposed method for calculating characteristic element lengths in mitigating mesh dependency.

3) The proposed framework successfully simulated quasi-brittle failure, as evidenced in the CT and TPB tests. It also demonstrated its applicability to brittle failure scenarios, as the FPB test shows.

4) The application of the NDK approach in the TPB and FPB tests demonstrated that carefully selecting non-critical zones can achieve results comparable to those of the cor-

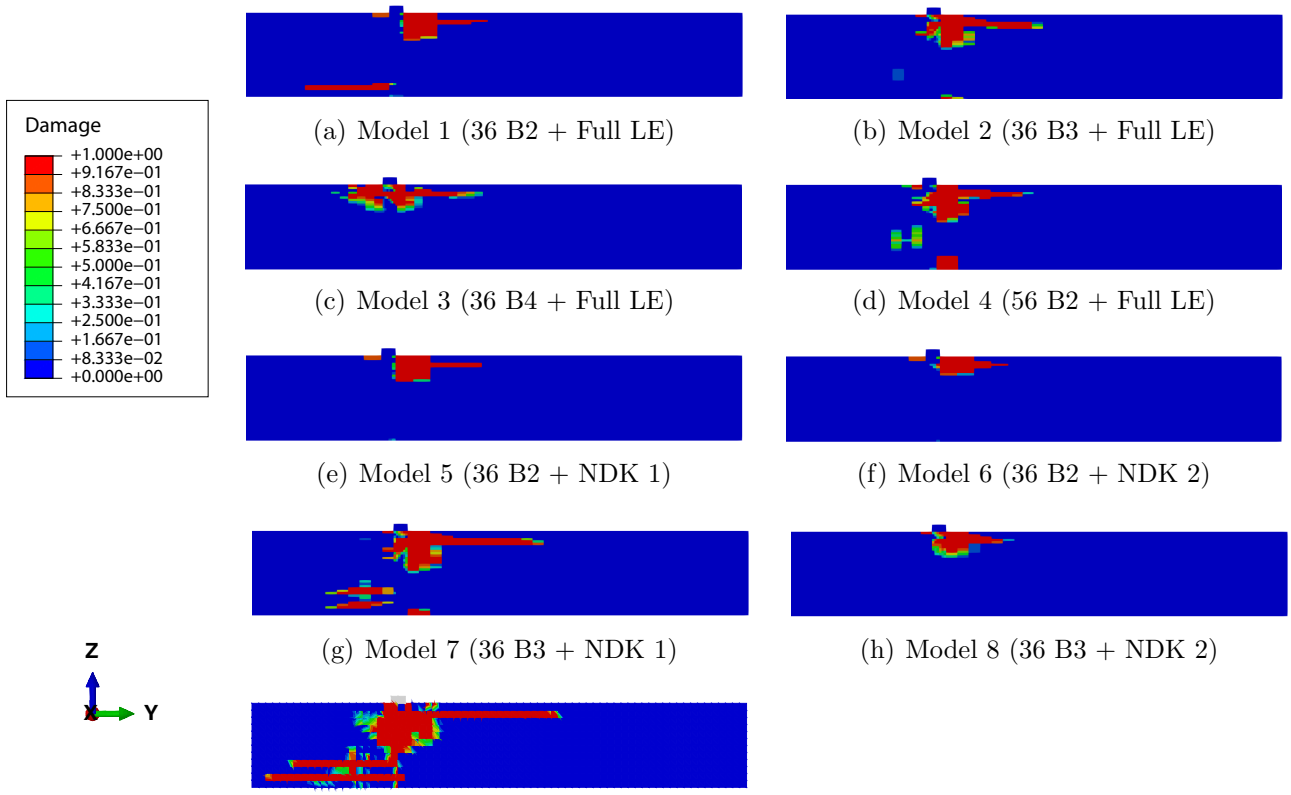

(a) Model 1 (36 B2 + Full LE)

(b) Model 2 (36 B3 + Full LE)

(c) Model 3 (36 B4 + Full LE)

(d) Model 4 (56 B2 + Full LE)

(e) Model 5 (36 B2 + NDK 1)

(f) Model 6 (36 B2 + NDK 2)

(g) Model 7 (36 B3 + NDK 1)

(h) Model 8 (36 B3 + NDK 2)

(i) ABQ 3D

Figure 23: Shear damage distribution of the FPB beam from various models

responding refined models. Additionally, incorporating a transition region using higher-order TE contributed to the balance between computational efficiency and accuracy.

5) Across the TPB and FPB tests, NDK models achieved at least a 50 % reduction in DOF without sacrificing too much accuracy compared to their refined counterparts. Moreover, there is still a potential for further reductions in the FPB test because a large number of beam elements were assigned.

6) The scalability of the NDK approach should be highlighted, allowing for straightforward enhancements to beam models by adjusting the cross-sectional kinematics at individual beam nodes without requiring remeshing. This feature demonstrates the adaptability of the proposed framework.

While the current NDK models demonstrate satisfactory performance, their accuracy still depends on manually defined non-critical, critical, and transition zones based on prior knowledge and trial-and-error. Future research may focus on incorporating automated optimization strategies, such as the best theory diagrams [54], for zone definition to maximize the potential of the proposed framework.

Acknowledgement

This research has received funding from the European Research Council (ERC) under the European Union's Horizon 2020 research and innovation program (Grant agreement No.

850437). The authors are also thankful for the support provided by the research projects 0305/1102/24160 MESTR - Modelação do Comportamento Estrutural and 0302/1102/24163 SEPINOV - Sistemas Estruturais e Produtos Inovadores from LNEC.

References

[1] S. W. Tsai, E. M. Wu, A general theory of strength for anisotropic materials, Journal of Composite Materials 5 (1) (1971) 58–80.

[2] Z. Hashin, Failure criteria for unidirectional fiber composites, Journal of Applied Mechanics (1980).

[3] A. Puck, H. Schürmann, Failure analysis of frp laminates by means of physically based phenomenological models, in: Failure criteria in fibre-reinforced-polymer composites, Elsevier, 2004, pp. 832–876.

[4] F. Nunes, M. Correia, J. Correia, N. Silvestre, A. Moreira, Experimental and numerical study on the structural behavior of eccentrically loaded gfrp columns, Thin-Walled Structures 72 (2013) 175–187.

[5] L. A. Fernandes, F. Nunes, N. Silvestre, J. R. Correia, J. Gonilha, Web-crippling of gfrp pultruded profiles. part 2: Numerical analysis and design, Composite Structures 120 (2015) 578–590.

[6] A. Matzenmiller, J. Lubliner, R. L. Taylor, A constitutive model for anisotropic damage in fiber-composites, Mechanics of Materials 20 (2) (1995) 125–152.

[7] K. V. Williams, R. Vaziri, Application of a damage mechanics model for predicting the impact response of composite materials, Computers & Structures 79 (10) (2001) 997–1011.

[8] P. P. Camanho, C. G. Dávila, Mixed-mode decohesion finite elements for the simulation of delamination in composite materials, Tech. rep. (2002).

[9] Z. P. Bažant, B. H. Oh, Crack band theory for fracture of concrete, Matériaux et Construction 16 (1983) 155–177.

[10] M. Laffan, S. Pinho, P. Robinson, A. McMillan, Translaminar fracture toughness testing of composites: A review, Polymer Testing 31 (3) (2012) 481–489.

[11] A. Ortega, P. Maimí, E. González, D. Trias, Characterization of the translaminar fracture cohesive law, Composites Part A: Applied Science and Manufacturing 91 (2016) 501–509.

[12] A. Ortega, P. Maimí, E. V. González, D. Trias, Specimen geometry and specimen size dependence of the r-curve and the size effect law from a cohesive model point of view, International Journal of Fracture 205 (2) (2017) 239–254.

[13] I. Lapczyk, J. A. Hurtado, Progressive damage modeling in fiber-reinforced materials, Composites Part A: Applied Science and Manufacturing 38 (11) (2007) 2333–2341.

[14] M. Arruda, L. Almeida-Fernandes, L. Castro, J. Correia, Tsai–wu based orthotropic damage model, Composites Part C: Open Access 4 (2021) 100122.

[15] Z. Xiong, C. Zhao, Y. Meng, W. Li, A damage model based on tsai–wu criterion and size effect investigation of pultruded gfrp, Mechanics of Advanced Materials and Structures 31 (3) (2024) 571–585.

[16] A. M. G. Coelho, J. T. Mottram, K. A. Harries, Finite element guidelines for simulation of fibre-tension dominated failures in composite materials validated by case studies, Composite Structures 126 (2015) 299–313.

[17] D. Robbins, J. Reddy, F. Rostam-Abadi, Layerwise modeling of progressive damage in fiber-reinforced composite laminates, International Journal of Mechanics and Materials in Design 2 (2005) 165–182.

[18] C. Hühne, A.-K. Zerbst, G. Kuhlmann, C. Steenbock, R. Rolfes, Progressive damage analysis of composite bolted joints with liquid shim layers using constant and continuous degradation models, Composite Structures 92 (2) (2010) 189–200.

[19] R. Gutkin, S. Pinho, Practical application of failure models to predict the response of composite structures, in: Proceedings of 18th international conference on composite materials, 2011.

[20] K. C. Warren, R. A. Lopez-Anido, S. S. Vel, H. H. Bayraktar, Progressive failure analysis of three-dimensional woven carbon composites in single-bolt, double-shear bearing, Composites Part B: Engineering 84 (2016) 266–276.

[21] B. Mandal, A. Chakrabarti, Simulating progressive damage of notched composite laminates with various lamination schemes, International Journal of Applied Mechanics and Engineering 22 (2) (2017).

[22] A. M. Girão Coelho, J. T. Mottram, Numerical evaluation of pin-bearing strength for the design of bolted connections of pultruded frp material, Journal of Composites for Construction 21 (5) (2017) 04017027.

[23] M. Akterskaia, P. P. Camanho, E. Jansen, A. Arteiro, R. Rolfes, Progressive delamination analysis through two-way global-local coupling approach preserving energy dissipation for single-mode and mixed-mode loading, Composite Structures 223 (2019) 110892.

[24] F. Zhuang, A. Arteiro, C. Furtado, P. Chen, P. P. Camanho, Mesoscale modelling of damage in single-and double-shear composite bolted joints, Composite Structures 226 (2019) 111210.

[25] D. Martins, J. Gonilha, J. R. Correia, N. Silvestre, Exterior beam-to-column bolted connections between gfrp i-shaped pultruded profiles using stainless steel cleats. part 1: Experimental study, Thin-Walled Structures 163 (2021) 107719.

[26] J. A. Gonilha, D. Martins, Numerical simulation of the damage progression of pultruded gfrp beam-to-column connections under monotonic and cyclic loads, Composite Structures 300 (2022) 116180.

[27] M. Arruda, M. Trombini, A. Pagani, Implicit to explicit algorithm for abaqus standard user-subroutine umat for a 3D hashin-based orthotropic damage model, Applied Sciences 13 (2) (2023) 1155.

[28] M. T. Arruda, Orthotropic damage model for composite structures using the 3D tsai-wu failure criterion, Mechanics of Advanced Materials and Structures 31 (27) (2024) 9584–9600.

[29] E. Carrera, M. Cinefra, M. Petrolo, E. Zappino, Finite element analysis of structures through unified formulation, John Wiley & Sons, 2014.

[30] J. Shen, M. T. Arruda, A. Pagani, Concrete damage analysis based on higher-order beam theories using fracture energy regularization, Mechanics of Advanced Materials and Structures 30 (22) (2023) 4582–4596.

[31] J. Shen, M. T. Arruda, A. Pagani, E. Carrera, A regularized higher-order beam elements for damage analysis of reinforced concrete beams, Mechanics of Advanced Materials and Structures 31 (1) (2024) 79–91.

[32] M. Nagaraj, J. Reiner, R. Vaziri, E. Carrera, M. Petrolo, Progressive damage analysis of composite structures using higher-order layer-wise elements, Composites Part B: Engineering 190 (2020) 107921.

[33] M. Nagaraj, J. Reiner, R. Vaziri, E. Carrera, M. Petrolo, Compressive damage modeling of fiber-reinforced composite laminates using 2d higher-order layer-wise models, Composites Part B: Engineering 215 (2021) 108753.

[34] A. Forghani, N. Zobeiry, A. Poursartip, R. Vaziri, A structural modelling framework for prediction of damage development and failure of composite laminates, Journal of Composite Materials 47 (20-21) (2013) 2553–2573.

[35] M. Trombini, M. Enea, M. Arruda, A. Pagani, M. Petrolo, E. Carrera, 1d higher-order theories for quasi-static progressive failure analysis of composites based on a full 3D hashin orthotropic damage model, Composites Part B: Engineering 270 (2024) 111120.

[36] E. Carrera, E. Zappino, One-dimensional finite element formulation with node-dependent kinematics, Computers & Structures 192 (2017) 114–125.

[37] E. Zappino, G. Li, A. Pagani, E. Carrera, Global-local analysis of laminated plates by node-dependent kinematic finite elements with variable ESL/LW capabilities, Composite Structures 172 (2017) 1–14.

[38] E. Carrera, E. Zappino, G. Li, Finite element models with node-dependent kinematics for the analysis of composite beam structures, Composites Part B: Engineering 132 (2018) 35–48.

[39] E. Carrera, A. Pagani, R. Augello, Large deflection of composite beams by finite elements with node-dependent kinematics, Computational Mechanics 69 (6) (2022) 1481–1500.

[40] D. Scano, E. Carrera, M. Petrolo, Use of the 3d equilibrium equations in the free-edge analyses for laminated structures with the variable kinematics approach, Aerotecnica Missili & Spazio 103 (2) (2024) 179–195.

[41] J. Shen, M. R. Tiago Arruda, A. Pagani, A consistent crack bandwidth for higher-order beam theories: Application to concrete, International Journal of Damage Mechanics 33 (4) (2024) 269–292.

[42] J.-L. Chaboche, Continuum damage mechanics: Part i—general concepts, Journal of Applied Mechanics (1988).

[43] M. Hinton, Failure criteria in fibre reinforced polymer composites: the world-wide failure exercise, Elsevier, 2004.

[44] S. W. Tsai, A survey of macroscopic failure criteria for composite materials, Journal of Reinforced Plastics and Composites 3 (1) (1984) 40–62.

[45] K.-S. Liu, S. W. Tsai, A progressive quadratic failure criterion for a laminate, Composites Science and Technology 58 (7) (1998) 1023–1032.

[46] S. Li, E. Sitnikova, Y. Liang, A.-S. Kaddour, The tsai-wu failure criterion rationalised in the context of ud composites, Composites Part A: Applied Science and Manufacturing 102 (2017) 207–217.

[47] C. Comi, U. Perego, Fracture energy based bi-dissipative damage model for concrete, International Journal of Solids and Structures 38 (36-37) (2001) 6427–6454.

[48] K. M. Mosalam, G. H. Paulino, Evolutionary characteristic length method for smeared cracking finite element models, Finite Elements in Analysis and Design 27 (1) (1997) 99–108.

[49] M. Jirásek, M. Bauer, Numerical aspects of the crack band approach, Computers & Structures 110 (2012) 60–78.

[50] L. Almeida-Fernandes, N. Silvestre, J. R. Correia, Characterization of transverse fracture properties of pultruded gfrp material in tension, Composites Part B: Engineering 175 (2019) 107095.

[51] W. Liu, P. Feng, J. Huang, Bilinear softening model and double k fracture criterion for quasi-brittle fracture of pultruded frp composites, Composite Structures 160 (2017) 1119–1125.

[52] J. R. Correia, D. Martins, J. Gonilha, M. Arruda, C. Andre, J. Nascimento, F. Branco, Clickhouse project an all composite emergency housing system, in: Proceedings of the Conference on Advances in Composite Materials and Structures, Instambul CACM, 2015.

[53] M. Arruda, L. Castro, A. Ferreira, D. Martins, J. Correia, Physically non-linear analysis of beam models using carrera unified formulation, Composite Structures 195 (2018) 60–73.

[54] M. Petrolo, P. Iannotti, Best theory diagrams for laminated composite shells based on failure indexes, Aerotecnica Missili & Spazio 102 (3) (2023) 199–218.